JOURNAL OF PETROLOGY

Journal of Petrology, 2022, Vol. 63, No. 3, 1–23
https://doi.org/10.1093/petrology/egac016
Advance Access Publication Date: 2 March 2022
Original Manuscript

OXFORD

Olivine Melt Inclusion Constraints on Some Intensive Properties of Subvolcanic Crystal Mushes and Their Evolution through Boundary Layer Fractionation in Northern Japan

R. Brahm[1,*], G. F. Zellmer[1], T. Kuritani[2], N. Sakamoto[3], H. Yurimoto[3], M. Nakagawa[2], and E. Sato[4]

[1]School of Agriculture and Environment, Massey University, Palmerston North 4442, New Zealand [2]Graduate School of Science, Hokkaido University, Sapporo 060-0810, Japan [3]Isotope Imaging Laboratory, Creative Research Institution, Hokkaido University, Sapporo 001-0020, Japan and [4] Hokkaido University of Education, Asahikawa 070-8621, Japan

*Corresponding author: Tel: (+64) 2102270893. E-mail: r.brahm@massey.ac.nz

Received 14 May 2021; Revised 26 January 2022; Accepted 25 February 2022

Abstract

Magma differentiation in arc settings has usually been attributed to an interplay of processes (fractional crystallization, assimilation, and magma mixing). Homogeneous fractional crystallization has been widely used to model the magmatic evolution of volcanic systems in arc settings due to its simplicity, even though boundary layer fractionation (BLF) has been proposed as a preponderant process of differentiation in hydrous magmatic systems. Both models produce distinct compositional paths and the application of the wrong model yields erroneous estimates of parameters like pressure–temperature-H_2O conditions and primary melt compositions. Melt inclusion (MI) populations corrected for post-entrapment processes have the potential to help discriminate between these two types of fractional crystallization, as their compositions are not affected by crystal accumulation and should capture the magmatic evolution as crystallization occurs. In this study, olivine-hosted MIs are used to assess the differentiation trends of basic arc magmas in northern Japan. Differentiation trends from five arc volcanic systems in northern Japan show that BLF is ubiquitous. Homogeneous fractionation models are unable to explain the liquid lines of descent of minor elements, like TiO_2 and P_2O_5. To reproduce these differentiation trends, the presence of accessory phases like titanomagnetite or apatite are required, which in many cases are not equilibrated by the melt or need to be fractionated in amounts that are incompatible with homogeneous fractionation. The prevalence of BLF in all studied arc magmas of northern Japan indicates that solidification fronts are key environments in the crustal evolution of some hydrous subduction zone magmas.

Key words: Kuril arc; north Japan arc; post-entrapment crystallization; fractional crystallization; magma differentiation

INTRODUCTION

The differentiation mechanisms of magmatic systems in the crust have been a crucial point of interest for many studies in igneous petrology and geochemistry (Harker, 1909; Bowen, 1928; Nielsen, 1990; Wilson, 1995; Dufek & Bachmann, 2010). These studies are particularly relevant in volcanic settings, as understanding the mechanisms involved in magmatic evolution can shed light into conditioning and triggering processes involved in hazardous volcanic eruptions (e.g., magma transport, pressure build-up, viscosity increase, volatile concentration, and volatile exsolution; Blake, 1984; Wotzlaw *et al.*,

2014; Gonnermann, 2015; Petrelli *et al.*, 2018). In general, from a geochemical perspective, the mechanisms of magma differentiation have been broadly described as an interplay of three main processes: (1) fractional crystallization (FC) or equilibrium crystallization; (2) assimilation; and (3) magma mixing, e.g. through periodic recharge.

In many cases, FC has been invoked as the main process of magma differentiation at crustal depths (e.g., Bowen, 1915; Yoshida & Aoki, 1984; Grove & Kinzler, 1986; Zen, 1986; Watanabe *et al.*, 2006; Gelman *et al.*, 2013; Kimura & Ariskin, 2014; Mollo *et al.*, 2015; Portnyagin *et al.*, 2015; Forni *et al.*, 2016; Gavrilenko *et al.*, 2016b; Brahm *et al.*, 2018). Most attempts to quantify FC have been performed by applying Rayleigh fractionation, which assumes that the crystallization process occurs homogeneously throughout the magmatic body (homogeneous FC (HFC); Nielsen & DeLong, 1992), usually using thermodynamic models of mineral-melt equilibrium (e.g., MELTS, COMAGMAT, Petrolog3; Ghiorso & Sack, 1995; Ghiorso *et al.*, 2002; Ariskin & Barmina, 2004; Danyushevsky & Plechov, 2011; Gualda *et al.*, 2012; Ariskin *et al.*, 2018). For its simplicity, this approach is commonly preferred over more complex fractionation models. However, HFC modelling does not assess for dynamic processes occurring within the magmatic body that can have strong effects on the compositional path of the melt, and it relies on a simplistic view of chamber-wide convection and/or crystal settling.

In contrast, several studies have proposed that crystallization of magma reservoirs dominantly operates in solidification fronts at their boundaries, where the magma is expected to cool most effectively (Langmuir, 1989; Nielsen & DeLong, 1992; Marsh, 1996; O'Hara & Fry, 1996; Kuritani, 1999; Marsh, 2007; Kuritani, 2009; Simura & Ozawa, 2011). Abundant crystallization in this boundary layer generates a mushy wall isolating the magma body from the wall-rock. The differentiated liquids generated in the boundary layer may be continuously transported to the main magma body through extraction processes from the boundary crystal mush (Bachmann & Bergantz, 2004; Bachmann & Bergantz, 2006; Pistone *et al.*, 2017). The chemical evolution of the magma can then be modelled by mixing of the central melt with increments of differentiated magma from the boundary layer (*in situ* crystallization or boundary layer fractionation (BLF); Langmuir, 1989; Nielsen & DeLong, 1992). The compositional path generated by BLF is substantially different to the one produced by HFC, mainly because the boundary layer crystallizes mineral phases that are not expected to be fractionated by the central melt. Hence, the application of HFC or BLF models can have strong discrepancies in the interpretation of magmatic conditions and discriminating between these processes is thus of crucial importance. BLF has been proposed to explain the compositional evolution observed in some volcanic suites (Kuritani, 1999; Kuritani, 2009) and has been shown to be compatible with field observations of sheet-like intrusive bodies (Simura & Ozawa, 2011).

As many volcanic rocks are crystal-rich, their compositions are usually affected by crystal accumulation processes and by entrainment of antecrysts and xenocrysts (e.g., Jerram & Martin, 2008; Zellmer *et al.*, 2014; Zellmer *et al.*, 2016). This makes it hard to identify from whole rock compositions the liquid line of decent of evolving magmas. Melt inclusions (MIs) have the potential to preserve the melt composition along the differentiation path as they are trapped in the crystalizing mineral phases, unaffected by contamination of other crystals. Nonetheless, there are a series of processes known to change MI composition after entrapment, such as post-entrapment crystallization (PEC) of daughter crystals or the host mineral from the MI boundary, diffusion of elements between MI and host, exsolution of volatile phases into a gas bubble, among others (Roedder, 1979; Danyushevsky *et al.*, 2000; Hartley *et al.*, 2015; Wallace *et al.*, 2015; Maclennan, 2017; Turner *et al.*, 2017b). Olivine-hosted MIs have been widely used due to their potential to preserve early-stage compositions, and their post-entrapment processes are comparatively well characterized (e.g., Danyushevsky *et al.*, 2002; Danyushevsky *et al.*, 2004; Kelley *et al.*, 2006; Rowe *et al.*, 2011).

In the present study, olivine-hosted MIs from five arc-front volcanic centres in northern Japan are analysed to study their differentiation paths and to identify the prevalence of HFC or BLF in each magmatic system. Results show that BLF might be a common process of magma differentiation in mafic arc-front magmas throughout northern Japan.

TECTONIC AND GEOLOGIC SETTING

The Hokkaido and Tohoku regions of Japan are located on the Okhotsk Plate, whereas SW Japan belongs to the Eurasian (or Amur) Plate. At the eastern margins of Hokkaido and NE Honshu, the Pacific Plate is subducted beneath the Okhotsk Plate (7–11 cm/yr; Northrup *et al.*, 1995; Bird, 2003), forming the Kuril (to the north) and Japan (to the south) trenches. In Hokkaido, the NE Japan arc meets the southernmost Kuril arc in an arc–arc collision zone (Kimura, 1996; Kita *et al.*, 2014), known as the Hidaka collision zone. Oblique subduction of the Pacific plate produces a southward migration of the Kuril fore-arc sliver (Fig. 1), which has been colliding with the NE Japan arc in south-central Hokkaido since Miocene times (*c.* 12 Ma), resulting in uplift of the Hidaka Mountains. There is a volcanic gap of *c.* 120 km between the two arcs, coincident with the collision zone. The orientation of the trench in the arc junction changes from N10E in the NE Japan arc to N56E in the Kuril arc, which leads to bending of the subducted slab. This bending has been associated with higher thermal inputs from the underlying mantle, caused by cracking or thinning of the subducted oceanic crust, which is thought to affect the slab-fluid input of magmatism generated above the slab-bending zone (Kuritani *et al.*, 2008; Kuritani *et al.*, 2016). Arc volcanism in NE Honshu and Hokkaido has been located in the same position for the last *c.* 5 Ma (Martin, 2011; Yoshida *et al.*, 2014). Caldera-dominated felsic volcanism related to NE–SW oriented compression shifted *c.* 2 Ma to a stratovolcano-dominated basaltic to andesitic volcanism associated with a change to a current ENE- to WSW-oriented compression in NE Honshu (Acocella *et al.*, 2008).

Five Holocene volcanic systems distributed along the Kuril and NE Japan arc fronts were chosen for this study (Fig. 1). These volcanic systems were selected to represent a wide distribution of magma generation along the arc front, with the condition that they have basic tephra products with olivine-hosted glassy MIs. The selected volcanic systems are Akita-Komagatake, Hakkoda, Tokachidake, Akan-fuji, and Tya-Tya. One tephra sample for each of these volcanic systems was analysed for the present study.

Akita-Komagatake

Akita-Komagatake is the southernmost volcano in this study, it is located in the Tohoku region and it belongs to the arc front section of the NE Japan arc. Its activity started at $\sim 74 \pm 15$ ka (Itaya *et al.*, 1984) and its eruptive history can be divided into three main stages (Sutō & Ishii, 1987): (1) stratocone formation stage, (2) syn-caldera stage, and (3) post-caldera stage. The compositions of Akita-Komagatake products range from basaltic to andesitic (Nakagawa, 1985; Sutō & Ishii, 1987; Fujinawa *et al.*, 2004; Ueki & Iwamori, 2017). The selected sample (AK) corresponds to the Hokubu 2nd

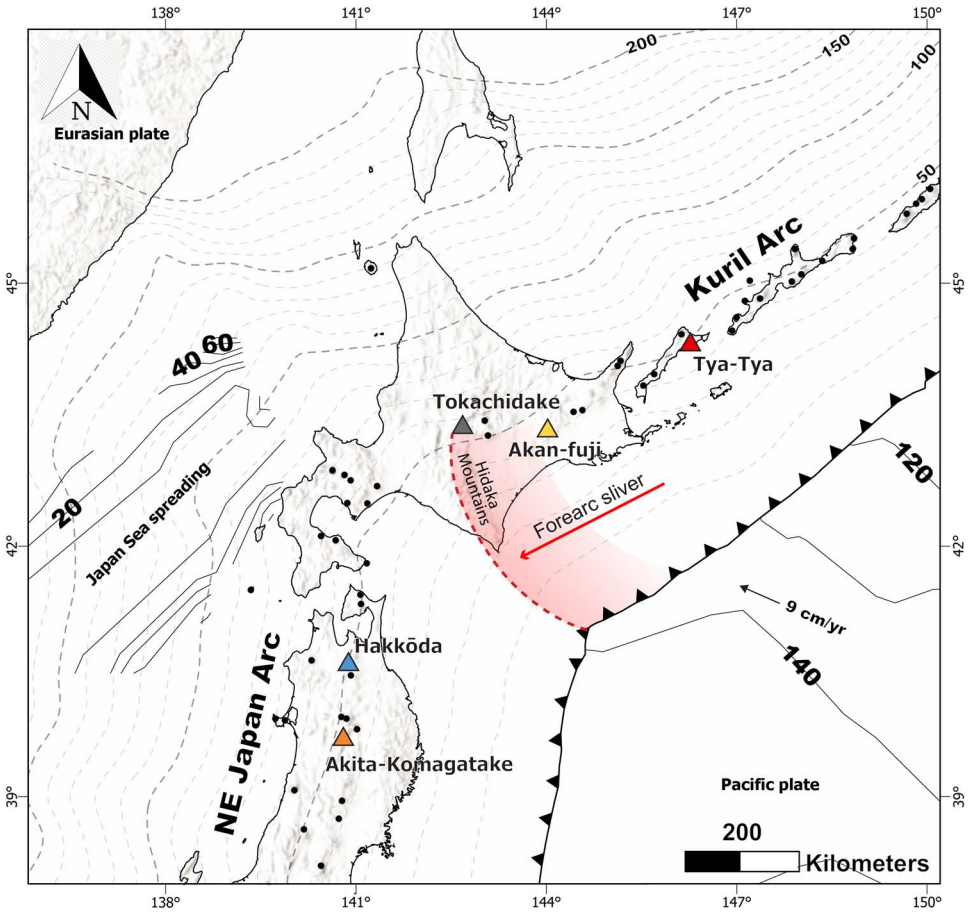

Figure 1 Topographic map of NE Japan. Triangles with names are the volcanic systems of interest in this study. Black dots are other volcanoes of the NE Japan and Kuril arcs. The black line with triangles marks the trench. The red area indicates the collision zone of the Kuril fore-arc sliver over the NE Japan arc, and the red arrow indicates its direction of movement. Grey dashed lines indicate the depth of the slab (in kilometre). The thin black lines indicate the age of the sea floor (in Ma).

pyroclastic cone deposits, believed to be associated with the *c*. 7 ka 'AK-6' tephra layer (Wachi & Koshiya, 1997;Fujinawa *et al*., 2004 ; Kuritani *et al*., 2019), which is the unit with the highest MgO content found in this volcanic system (Fujinawa *et al*., 2004; Kuritani *et al*., 2019).

Hakkoda

Hakkoda (or Kita-Hakkoda) is the northernmost volcano from the arc front of the NE Japan volcanic arc in this study and is located south of Mutsu Bay in northern Tohoku. It is part of the Hakkodasan volcanic area that comprises at least 17 stratovolcanoes and lava domes, divided in the Kita-Hakkoda volcanic group (north) and Minami-Hakkoda volcanic group (south). Hakkodasan products range from basalts to dacites (49.4 and 63.2 wt% SiO_2) (Sasaki *et al*., 1985; Sasaki, 1986; Sasaki, 1987). The current volcanic activity is located in Kita-Hakkoda, which has been active since 0.4 Ma (Kudo *et al*., 2004; Takarada & Muraoka, 2004). Historic activity of Kita-Hakkoda has only involved seismic swarms (1986) and volcanic gas emanations (1997 and 2010) (Kudo & Hoshizumi, 2006). Past eruptions include five magmatic to phreatic eruptions of Odake volcano from 4.8 to 1.5 ka and three phreatic eruptions of Jigokunuma crater from 0.7 to 0.4 ka. The tephra sample in this study (HK) corresponds to tephra fall from the 2 ka Odake phreatomagmatic eruption HK-2 (Kudo *et al*., 2000; Kudo *et al*., 2003; Kudo *et al*., 2004).

Tokachidake

This volcanic system is the southernmost volcano in the Kuril arc. It is located in the south-westward collision zone of the Kuril forearc sliver over the NE Japan arc forearc, generating a 120-km volcanic gap between the Kuril and NE Japan arcs (Kita *et al*., 2012). The eruptive history of TK is divided into Older (1.0–0.5 Ma), Middle (300–70 ka), and Younger (60–50 ka to present) stages (Ishizuka *et al*., 2010). Tokachidake is the central stratovolcano where most of the activity of the Younger stage occurred, starting with andesitic to dacitic products. Later activity was dominated by fall deposits and lava flows, with lesser amounts of pyroclastic flow deposits. Historic eruptions in the 20th century occurred in 1926, 1962, and 1988–1989 (Nakagawa *et al*., 2019). The TK sample from this study belongs to a proximal fall deposit of the 1962 sub-plinian eruption.

Akan-Fuji

Akan-fuji is located in NE Hokkaido in the south Kurile arc front. It is one of the eight small stratovolcanoes that compose Meakandake (Yokoyama *et al*., 1976), located on the SW flank of the Akan caldera. Activity of Akan-fuji started ~1.0–2.5 ka ago, forming basaltic lavas and scoria fall deposits (Wada, 1997; Wada *et al*., 1998). The AKN sample was collected from fall deposits of the cone.

Tya-Tya

This stratovolcano is located in the north of Kunashir Island, the first volcanic island of the Kuril arc north of Hokkaido. Its development can be divided in the construction of an old and a young volcanic edifice (Nakagawa *et al.*, 2002), with the later partially overlying the former. Both volcanic edifices are compositionally distinct, where the old is composed of low-K products and the young is constituted by medium-K products. The last known activity occurred in 1973 forming two maars in the northern flank of the edifice through phreatic eruptions (Markhinin *et al.*, 1974), followed by the formation of two scoria cones in the southern flank. The largest scoria cone was the last one produced and represents the most active period of the 1973 eruptive sequence and within the southern Kuril arc in the 20th century, corresponding to a sub-Plinian eruption. Whole rock compositions of the young edifice of Tya-Tya range from tholeiitic basalt to dacite (49–63 wt% SiO_2) (Nakagawa *et al.*, 2002). Products from the 1973 eruption are crystal-poor, with a narrow compositional range of ~53–54 wt% SiO_2 (Nakagawa *et al.*, 2002). The selected sample (TT) was collected from the 1973 eruption scoria fall deposit (locality 6 in Nakagawa *et al.*, 2002).

ANALYTICAL METHODS

Whole rock major element analysis

Glass beads were prepared from whole rock powder of each tephra sample to perform x-ray fluorescence (XRF) analysis. The samples were cleaned in an ultrasonic bath with distilled water and dried in an oven at 100°C for at least 2 h. The samples were then powdered using a tungsten grinding machine and dried again in the oven at 100°C for at least 2 h. To determine loss on ignition, *c.* 2 g of powder was weighted before and after heating in an oven at *c.* 900°C for 3 h. After heating, *c.* 0.8 g of each powdered sample was mixed with *c.* 8.0 g of lithium metaborate, lithium tetraborate (12: 22) flux mixture, and then fused to produce a glass disc using a XRFuse2 electric fusion apparatus.

Major element concentrations were measured with a 1 kW Bruker Tiger S8 Series II XRF spectrometer at Massey University in Palmerston North, New Zealand. Interference-corrected spectra intensities were converted to oxide concentrations using calibration curves consisting of natural standards, closely approximating the mafic matrix of our samples. The long-term reproducibility of Oreas 24c standard reference material is better than ±1% relative (1σ) for all elements except MnO, for which it is better than ±1.5% relative.

Mineral and glass textural and compositional analysis

Textural features of the tephra samples were assessed through BSE imaging. BSE images of the exposed MIs were obtained using a JEOL JSM-7000F field emission scanning electron microscope (FE-SEM) at Hokkaido University, Japan. An acceleration voltage of 15 kV was used, with a beam current of 10 nA.

BSE images of thin sections and mineral and glass compositions were obtained using a JXA-8230 SuperProbe Electron Probe Microanalyser (EPMA) at Victoria University, New Zealand. Plagioclase crystals were analysed using a defocused beam of 10-μm diameter with an acceleration potential of 15 kV and an electron beam current of 12 nA. Olivine, pyroxene, and Fe-Ti oxide crystals were analysed using a focused beam with an acceleration potential of 20 keV and an electron beam current of 30 nA. Counting times were 40 s on peak and 15 s on background for all elements. Secondary standards were analysed periodically during the runs to constrain precision and accuracy and to assess for possible drift effects. Drift correction was applied for some of the analysis runs that showed drifting effects. Precision and accuracy evaluation for these mineral phases can be found in the Supplementary Material.

For MI olivine host crystals, analysis spots were chosen in the vicinity of the MIs to better constrain equilibrium conditions. A focused beam with acceleration potential of 20 keV was used with an electron beam current of 30 nA for Si, Fe, Mg, Mn, and Ti and 100 nA for Al, Ni, Ca, and Cr. Counting times were 40 s on peak and 15 s on background for all elements but Ca, with 400 s on peak and 20 s on background. Primary standards for olivine analysis were the Springwater olivine for Si, Fe, and Mg, wollastonite for Ca and synthetic pure oxides for Ti, Ni, Mn, and Cr. Accuracy and reproducibility of the analyses were constrained by alternated analysis of USNM2566 and JK3 olivine secondary standards during the session. Concentrations are accurate to <4% for major elements, < 35% for Mn, < 24% for Ni, and < 89% for Cr. Accuracy of Ca was usually <4% with a couple of analyses with *c.* 7%. Ti and Al values are usually below the detection limits for both standards. Reproducibility estimates (as 1σ) were <2% for major elements, *c.* 3% for Ni and Ca, *c.* 5% for Mn and *c.* 27% for Cr.

MI and interstitial glass compositions (Si, Ti, Al, Fe, Mn, Mg, Ca, Na, K, and P or Cr) were analysed with an accelerating potential of 15 keV and an electron beam current of 8 nA. A defocused beam of 5–10-μm diameter was used, and Na was analysed for 10 s first to avoid Na migration. Primary standards for glass analysis were the basaltic glass VGA99 for Si, Al, Fe, Mg, and Ca, the rhyolitic glass VG568 for Na and K, the Beeson apatite for P, and synthetic pure oxides for Ti, Mn, and Cr. Basaltic glass secondary standards (VGA99 and BHVO-2G) were analysed periodically throughout the session to test for instrumental drift and to constrain accuracy and reproducibility of the analyses. Reproducibility estimates (1σ) are <1% for SiO_2, Al_2O_3, and CaO, *c.* 2% for FeO and MgO, *c.* 3% for Na_2O and K_2O, *c.* 10% for TiO_2, MnO and P_2O_5. Accuracies uncertainties are <1% for most SiO_2 and Al_2O_3 secondary standard analyses, <2% for most Al_2O_3, FeO, MgO, and CaO analyses, <3% for most K_2O analyses, <10% for most Na_2O and TiO_2, analyses and <20% for most P_2O_5 analyses.

Glass H_2O and CO_2 analysis by secondary ion mass spectrometry

Volatile element analyses (H and C) of MI glasses were carried out with the Cameca ims-1270 secondary ion mass spectrometry (SIMS) at Hokkaido University, Japan. Exposed MIs were pressed down into an indium plug mounted in an aluminium disk to avoid H and C contamination from epoxy. The plug was then coated with gold and loaded into the SIMS to remain under vacuum for three days before analysis to reduce potential H contamination on the sample surface.

A Cs^+ ion primary beam was used to analyse for ^1H, ^{12}C, and ^{30}Si. Pre-sputtering of a 25 × 25-μm area was conducted before each analysis with beam current of 1 nA for 100 s, plus a beam centring time of 96 s. Analysis was carried out with a beam current of 0.1 nA in a 3–5 μm wide area of Gaussian shape. Field aperture was set to 2000 μm with an entrance slit of 60 μm, an energy slit of 25 μm, a contrast aperture of 100 μm, and an exit slit of 400 μm. Mass resolution was set to 3243 to avoid interference of isotopic signals. The isotopes were measured in five consecutive cycles of 10 s of waiting time and 3 s of analysis time for ^1H, 4 s waiting time and 5 s analysis time for ^{12}C, and 2 s waiting time and 1 s analysis time

for ^{30}Si. The reproducibility of counts ratios between each volatile and matrix was obtained from the five cycles per analysis. Maximum uncertainties of reproducibility are <10% for ^{1}H/^{30}Si and <13% for ^{12}C/^{30}Si.

Reference glasses were polished and mounted in the same indium plug with the MIs and were repeatedly measured during the same analysis session to produce the calibration lines and to check for instrument drift. The reference glasses used were BIR-1G and BHVO-2G synthetic standard glasses (USGS), plus CL DR-1, LS 427, 2πD43, SAM 76-11, and SAM 73-12 natural volcanic glasses (Kendrick *et al.*, 2017). H_2O and CO_2 compositions for most of the reference materials were measured using a micro-FTIR instrument at Massey University, Palmerston North. Conditions of H_2O and CO_2 analyses, plus the final reference materials compositions used for SIMS calibration can be found in the Supplementary Material. Calibration of the SIMS analyses was produced using a maximum likelihood linear regression scheme considering the uncertainties related to SIMS analysis precision and uncertainties in the reference values used. After calibration, the uncertainties in accuracy (1σ) for the volatile species in MIs are *c.* 4% for H_2O and <15% for CO_2 (for concentrations above 50 ppm). Detailed information of the SIMS counts results, calibration curves, MIs volatile concentrations and associated errors can be found in the Supplementary Material.

RESULTS

Petrography and mineral chemistry

Akita-Komagatake

The AK tephra sample is composed of a glass-rich groundmass (*c.* 75 vol% on a vesicle free basis) with plagioclase (Pl; *c.* 87 vol% of crystal cargo), olivine (Ol; *c.* 12 vol%) and scarce clinopyroxene (Cpx; < 1 vol%) phenocrysts (Fig. 2A). Present crystal clots are usually composed of a single mineral phase, with the exception of some scarce Ol + Cpx clots.

The AK sample Ol crystals have very homogeneous core compositions ($Fo_{77.4–78.5}$) with narrow less forsteritic rims (AK-Ol1 in Fig. 3A). These Ol crystals are the hosts of glassy MIs, are euhedral to subhedral and have sizes of *c.* 100 to 500 μm. They are present as isolated crystals or as small clots of Ol and scarce Cpx. Ol crystals of <100 μm in size are found also associated with small Cpx crystals and in contact with the rims of big Pl crystals (AK-Ol2). These smaller Ol crystals have slightly more Fe-rich compositions ($Fo_{74–77}$).

The Pl phenocrysts reach a maximum size of *c.* 2.5 cm and most of them are composed of a wide An-rich core ($An_{76–91}$; AK-Pl1 in Fig. 3B) and a narrow less anorthitic rim ($An_{65–75}$; AK-Pl2). The Pl cores usually present oscillatory zoning and resorption and regrowth textures. Some cores also host MIs or have sieve texture. Rims display oscillatory or normal zoning.

The Cpx crystals are augites (Aug) that are usually small (< 100 μm) and found associated with the group of smaller Ol crystals. They are typically zoned with low-Ca compositions towards the rims. The Cpx crystals are then divided into two compositional groups regarding their Ca content: the high-Ca group related to the cores (AK-Px1 in Fig. 3C) and the low-Ca group related to the rims in zoned crystals (AK-Px2).

Hakkoda

The HK tephra sample is composed of a crystal-rich groundmass (*c.* 71 vol% on vesicle free basis), hosting larger Pl (*c.* 84 vol% of the crystal cargo), Ol (*c.* 4 vol%), and pyroxene (Px; *c.* 12 vol%) crystals (Fig. 2B). Crystal clots formed by all mineral phases present in this rock are very common.

HK have two distinct Ol compositional groups. The most abundant group has a composition of $Fo_{76.4–79.7}$ (HK-Ol1 in Fig. 3A), which consists by normally zoned Ol crystals usually found in big crystal clots with Pl, Cpx, and Opx. Most MIs were found on Ol hosts of this group. The second group corresponds to Ol compositions of $Fo_{68.8–73.1}$ (HK-Ol2), which are mostly related to Ol remnants found inside big Opx crystals and Ol crystals with Opx coronas.

The largest Pl crystals reach *c.* 3 mm in size and present a texture similar to the Pl phenocrysts of the AK sample (Fig. 2E). They are composed of a wide core of $An_{84–95}$ (HK-Pl1 in Fig. 3B) with common resorption textures and oscillatory zoning and a narrow rim of $An_{70–81}$ (HK-Pl2).

Both Opx and Cpx are abundant and common constituents of crystal clots and are also found as isolated crystals. Px crystals are classified into three compositional groups. The most abundant compositional group, HK-Px1 (Fig. 3C), corresponds to most phenocrysts found in HK, which include the high-Mg and high-Ca Aug and their rims of low-Ca and low-Mg. The HK-Px2 group mainly consists of Opx and scarce Cpx related to crystals associated with coronas and reaction rims around Ol crystals of HK-Ol2 and overlaps in composition with the low-Ca and low-Mg compositions of HK-Px1. The HK-Px3 group consists of Cpx and Opx crystal cores of higher Fe content, which are surrounded by more Mg-rich regrowth zones represented by HK-Px1.

Tokachidake

The TK tephra sample is constituted by a glass-rich groundmass (*c.* 61 vol% on a vesicle free basis) and phenocrysts of Pl (*c.* 75 vol% of the crystal cargo), Cpx (*c.* 11 vol%), Ol (*c.* 7 vol%), titanomagnetite (T-Mag; *c.* 6 vol%), and scarce Opx. Crystal clots are very common and can be composed of all mineral phases found in this sample.

As with the previous tephra sample, Pl phenocrysts are constituted by a wide An-rich core ($An_{87–91}$; TK-Pl1 in Fig. 3B) with common sieve texture, oscillatory zoning, or resorption and regrowth textures, followed by narrow rims of $An_{72–79}$ (TK-Pl2).

TK also has two distinct Ol compositional groups (Fig. 3A). The higher forsterite group ($Fo_{74.0–77.6}$) corresponds to the bigger isolated crystals that host the MIs with homogeneous core compositions and narrow normal zoned rims. The second compositional group ($Fo_{67.8–71.3}$) includes smaller euhedral crystals associated with clots with pyroxene and Ti-Mag (Fig. 2C), anhedral crystals with Opx and Cpx coronas and Ol inclusions in Cpx crystals.

Aug is the most abundant pyroxene phenocryst type. It is present as large subhedral crystals with Ol inclusions in Cpx + Ti-Mag crystal clots and small anhedral crystals in Ol + Cpx + Ti-Mag crystal clots (TK-Px1 in Fig. 3C). Aug crystals with lower Ca content and scarce Opx are present as coronas surrounding anhedral Ol crystals (TK-Px2).

Akan-Fuji

Two main types of rock fragment types are present in the AKN tephra sample. Fragment type 1 consist of a crystal-rich groundmass (*c.* 48 vol% on a vesicle free basis) mainly composed of Pl, pigeonite (Pgt) and Ti-Mag, with Ol (*c.* 4 vol% of the crystal cargo) and Pl (*c.* 96 vol%) phenocrysts. Fragment type 2 has a glass-rich groundmass (*c.* 75 vol% on a vesicle free basis) with Pl (*c.* 86 vol% of the crystal cargo), Ol (*c.* 13 vol%), and Px (<1 vol%) phenocrysts.

The Pl phenocryst of the AKN sample can also be divided into two main groups (Fig. 3B). One with a wide An-rich core ($An_{81–95}$) with

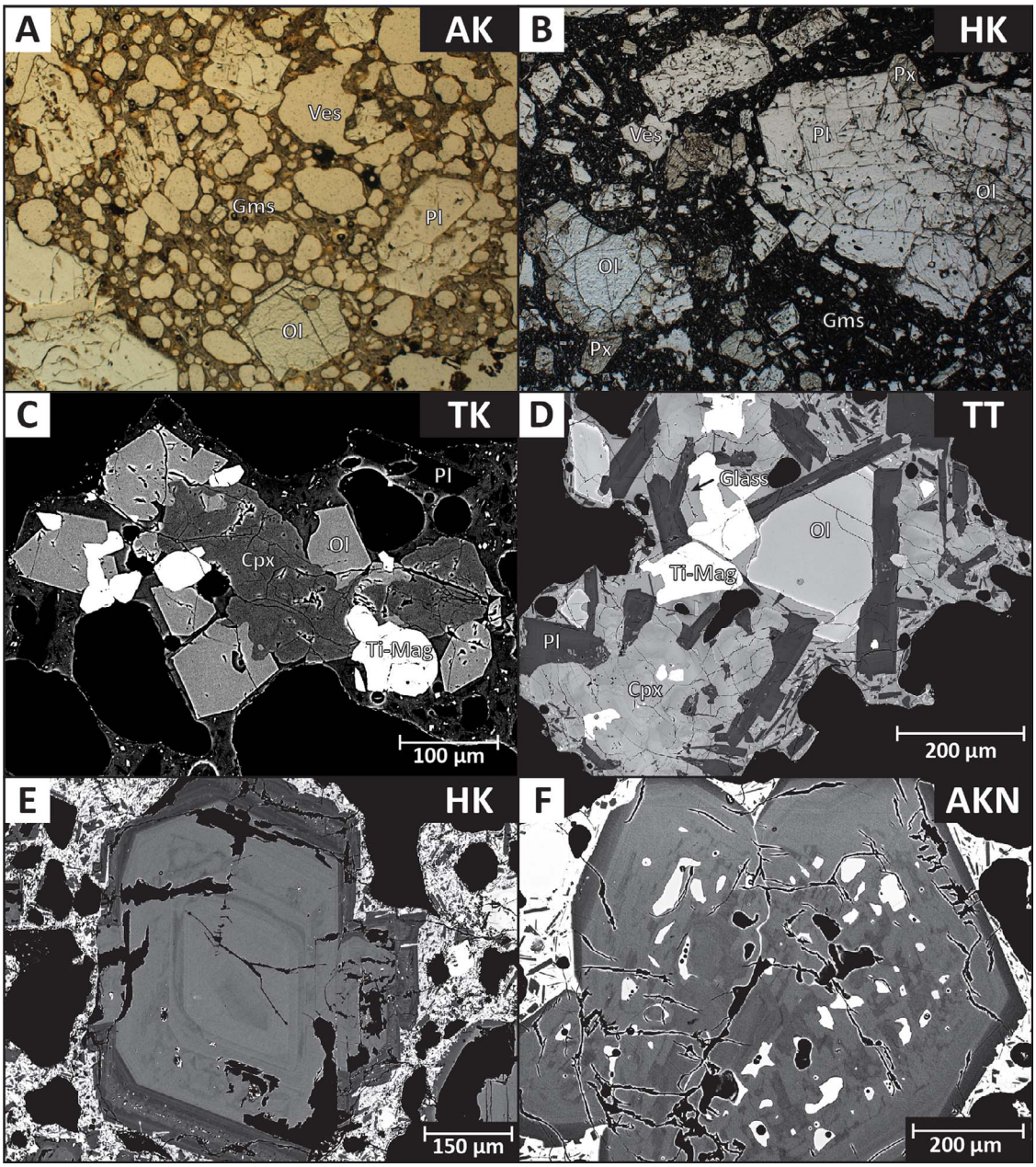

Figure 2 (A) and (B) Thin section microphotographs (parallel light) of AK and HK tephras. (C) and (D) BSE images of crystal clots from TK and TT sample. (E) and (F) BSE images of characteristic plagioclase texture found in all samples: wide An-rich core with narrow An-poor rim (see text).

common oscillatory zoning and sieve texture that is surrounded by a narrow less anorthitic rim ($An_{60–75}$) (Fig. 2F). And another found in fragments of type 1, where cores are homogeneous are normally zoned, without displaying any disequilibrium textures.

Unlike the other samples, AKN presents a wide range of Ol compositions (Fig. 3A). The higher Fo group ($Fo_{71–82}$ AKN-Ol1) corresponds to the Ol crystals found in fragments of type 2. They are represented by euhedral to subhedral crystals, isolated or in Ol + Pl clots, and by anhedral crystals in Cpx + Ol clots. Most core compositions of these crystals are homogeneous with slight normal zonation in the rims. A few crystals found in this sample present a normally zoned core followed by inverse zonation towards the rim. The AKN-Ol2 group consists mainly in low Fo ($Fo_{58–71}$), normally zoned Ol crystals with Pgt coronas found in fragments of type 1. This Ol group also includes olivine inclusions in big Px crystals.

Px crystals found in type 1 fragments show widespread disequilibrium textures. Cpx and Opx are found constituting the same big tabular Px crystals as patches of contrasting Ca content (AKN-Px2 in Fig. 3C). These crystals have Pgt rims of the composition of groundmass Pgt crystals and Ol inclusions. Opx is also found as reaction patches in some Ol crystals in type 1 fragments. Cpx is found in Cpx + Ol + Pl crystal clots of type 2 fragments (AKN-Px1). Some of these Cpx in clots include scarce and small Opx patches.

Tya-Tya

The TT sample has the lowest crystallinity of all five tephra samples (*c.* 84 vol% groundmass on a vesicle free basis). The crystal cargo is

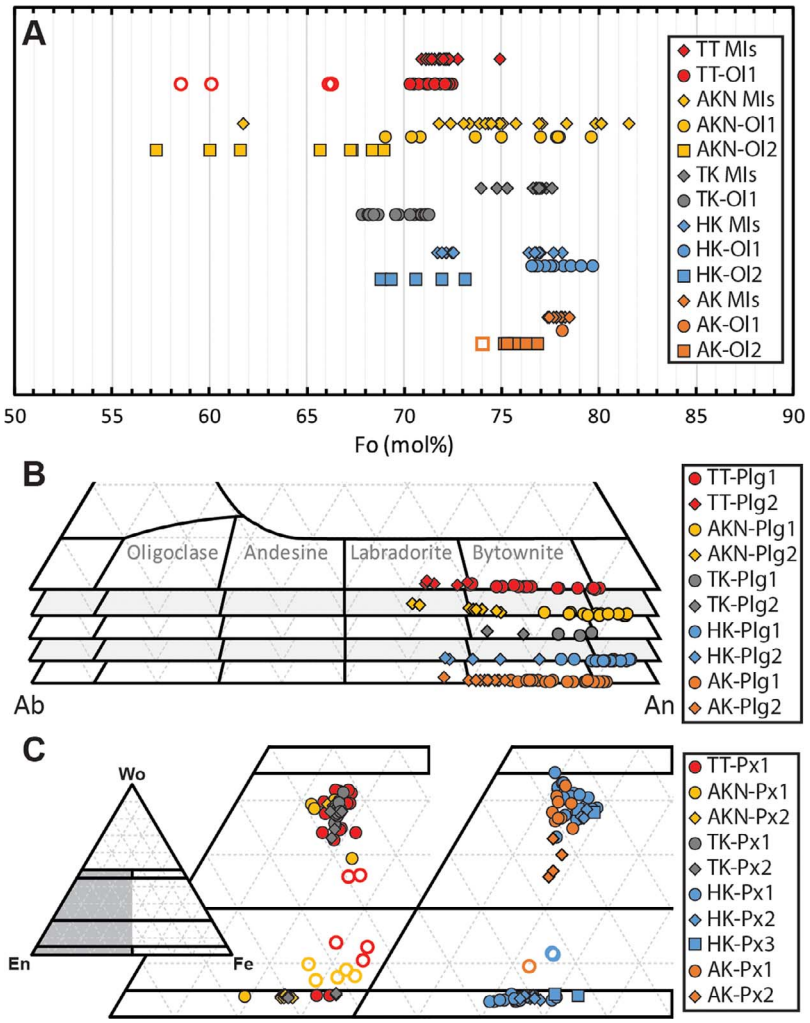

Figure 3 Compositions of (A) olivine, (B) plagioclase, and (C) pyroxene crystals for the five tephra samples. Each colour represents one of the volcanic systems following the same colour scheme as in Fig. 1. Hollow symbols indicate groundmass or outer rim compositions related to the ascent and eruption event. Compositional groups are defined in the main text. Diamonds in (A) indicate the olivine compositions of the crystals hosting MIs and can belong to any of the olivine groups defined from the thin sections. Uncertainties (1σ) are smaller than the symbol size.

composed of Pl (*c*. 77 vol% of crystal cargo), Px (*c*. 9 vol%), Ti-Mag (*c*. 8 vol%), and Ol (*c*. 6 vol%). Crystal clots of Ol + Cpx + Plg + Ti-Mag are abundant in this sample.

The Pl phenocrysts of the TT sample have textures similar to those in the other samples. Big plagioclase phenocrysts are composed of a wide An-rich core ($An_{74–90}$); TT-Pl1 surrounded by narrow An-poor rims ($An_{63–70}$); TT-Pl2. This type of plagioclase is associated to clots with smaller Ol, Cpx, and Ti-Mag crystals growing from their rims in contact with the An-poor section of the Pl crystals. There is another Pl group associated with the crystal clots. This group consists of smaller elongated crystals in clots, similar in sizes to the other mineral phases in the clots (Fig. 2D). These plg crystals display oscillatory zoning of $An_{63–70}$.

Ol phenocrysts found in this sample have a narrow compositional range of $Fo_{70.3–72.8}$, with an outlier of Fo_{75}. Ol phenocrysts are usually present as subhedral crystals in crystal clots, in some cases with embayment textures. Ol core compositions are homogeneous with narrow less forsteritic rims. Few Ol crystals show a wider Fo-rich rim with the development of a Pgt corona.

Px phenocrysts consists mostly of Aug with scarce Opx. They usually are associated with Ol + Pl + Cpx + Ti-Mag clots, but the largest crystals found are associated with Ol-free clots. Px compositions are shown in Fig. 3C.

MI textures

Most analysed MIs are glassy with no daughter minerals and with a shrinkage bubble (Fig. 4). Table 1 shows the number of MIs for each sample, the size range for the MIs, their shrinkage bubbles, and their Ol hosts.

Unlike the other samples, the TK MI population is not completely glassy. Most of these MIs contain a big Fe-Ti oxide crystal (Fig. 4B), which given their size, may have been entrapped during MI formation. Some Px daughter crystals nucleated from the Fe-Ti oxide walls, which may have affected the glass compositions measured in the TK MIs in some cases. Details of MI geometry, including volumes and BSE and optical microscope images can be found in the Supplementary Material.

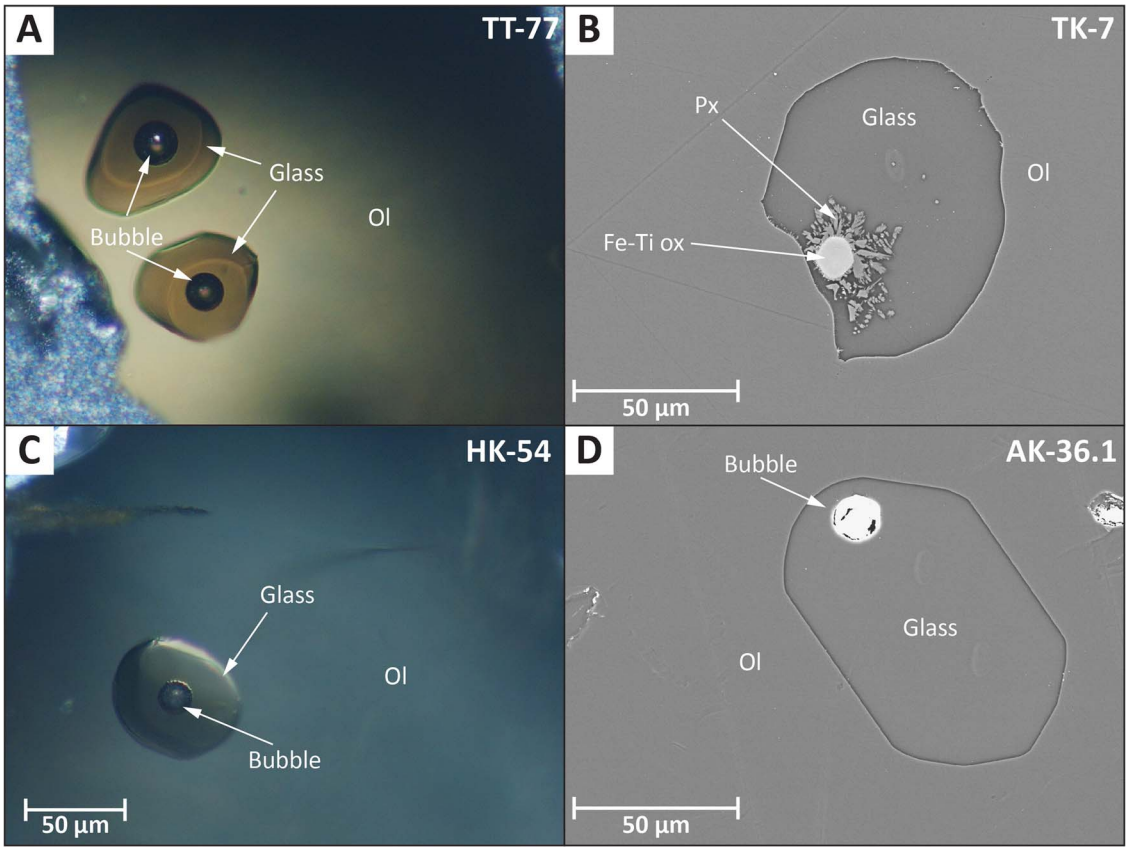

Figure 4 (A) and (C) show microphotograph of melt glassy inclusions in an olivine crystal with shrinkage bubbles. (B) BSE image of exposed MI from the TK sample with a Fe-Ti oxide crystal from where daughter pyroxene crystals grew. (D) BSE image of an exposed glassy MI from the AK sample.

Table 1: Number of MIs and size ranges of each sample

Sample units	Quantity MIs	Bubble % of MI volume	Size ranges MI μm^3	Ol host μm^3
AK	19	3.2–4.8	2.1×10^3–9.4×10^6	2.4×10^8–8.6×10^8
HK	13	1.6–3.9	2.3×10^4–1.0×10^7	1.4×10^8–2.5×10^9
TK	20	1.4–10.6	1.5×10^4–2.7×10^7	6.2×10^7–1.2×10^{10}
AKN	27	0.0–5.9	1.1×10^4–1.1×10^6	4.1×10^7–5.5×10^8
TT	26	2.8–4.4	1.5×10^4–2.3×10^6	2.4×10^7–$4.0 \times 10^{8*}$

*Except one outlier host at 1.8×10^9 μm^3.

Whole rock and glass geochemistry

All tephra samples are subalkaline and have basaltic to basaltic-andesitic compositions (*c.* 50.8 wt% to *c.* 52.8 wt%; Fig. 5). The samples from the NE Japan arc (AK and HK) are low in alkalis (*c.* 2 wt% $Na_2O + K_2O$), with a tholeiitic signature. The available glass compositions of HK and AK (Ol-hosted MIs, Pl-hosted MIs and groundmass) are all richer in SiO_2 than the whole-rocks. The Kuril arc samples have a calc-alkaline signature, with higher alkali concentrations (*c.* 3 wt% and *c.* 3.7 for TT and TK). The glass compositions from the Ol-hosted MIs of these samples overlap in composition with the whole-rock, whereas Pl-hosted MIs and groundmass glass of TT are more differentiated. The MI glass major elements compositions are listed in Table 2. All compositional data can be found in the Supplementary Material. Most MI glass analyses have totals of <100 wt% (majors + volatiles) down to *c.* 97 wt%. These discrepancies can be explained by the combination of volatile and trace components unaccounted here and the effect of sub-surface charging during EPMA analysis (Hughes *et al.*, 2019). Further details of these discrepancies are discussed in the Supplementary Material.

DISCUSSION

MI corrections

Corrections were performed to each MIs to estimate pre-eruptive compositions of major and volatile components. The term 'pre-eruptive' is used here instead of 'initial' for the corrected MI compositions because, as it is discussed below, in most samples the MIs and their host show evidence of being completely re-equilibrated with the surrounding melt to fixed Mg# (magnesium number) in equilibrium with a narrow range of Fo values. As the process of MI correction

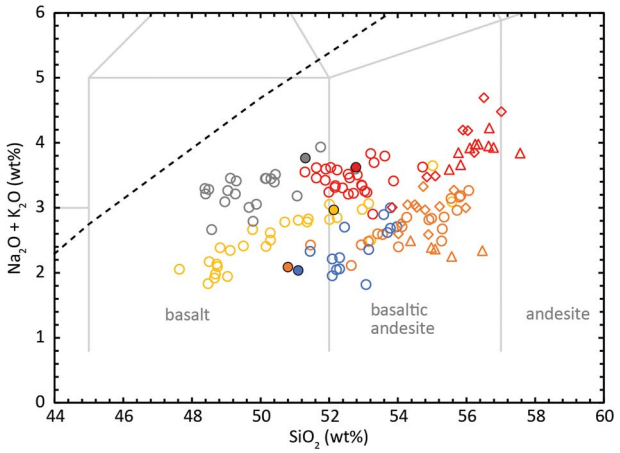

Figure 5 TAS diagram showing the whole rock and glass compositions of the five tephra samples. Colour scheme is the same as in Fig. 1. Filled circles are the whole-rock compositions. Hollow circles are the measured glass compositions of Ol-hosted MIs, diamonds are the glasses from Pl-hosted MIs, and triangles are glass compositions from the groundmass. Uncertainties (1σ) are smaller than the symbol size.

reconstructs the composition to its last stage of equilibrium, the results are interpreted as the compositions at storage conditions before remobilization and eruption (Brahm *et al.*, 2021).

A modified version of the MIMiC program (Rasmussen *et al.*, 2020) was used to apply a combined correction scheme for PEC, Fe-loss, CO_2 loss to the shrinkage bubble, and H_2O diffusive loss. MIMiC combines the classic PEC corrections schemes for Ol-hosted MIs (for PEC and Fe-loss) in a similar manner as previously applied with the Petrolog3 program (Danyushevsky & Plechov, 2011): equilibrium Ol is added to the MI composition until reaching equilibrium with the host Ol. Fe-loss is adjusted by iterative steps of Fe-Mg exchange and Ol addition until the iron content defined by the user is reached (see details in Danyushevsky *et al.*, 2000, Rasmussen *et al.*, 2020). The Mg-Fe distribution coefficient ($K_D{}^{Mg-Fe}_{Ol-melt}$) is calculated with the Toplis (2005) model and the temperature is estimated using the Ol-melt thermometer of Putirka *et al.* (2007). The Fe^{3+} content of the melt is treated as an incompatible component during Ol crystallization in a closed system. The biggest MI in each sample, which have flat BSE grey scale profile plateaus and are coincident with the MI predicted to have the least PEC are used to adjust the f_{O_2} conditions of the melt. The Fe speciation of each MI in a sample is set to the value for which 0 wt% of PEC is predicted for the MI expected to have suffered negligible PEC. At higher oxidation conditions PEM would be required, whereas PEC estimates would increase at lower f_{O_2}.

Blundy *et al.* (2020) produced a new parametrization of Mg-Fe_T partitioning ($K_D{}^{Mg-Fe_T}_{Ol-melt}$) and combined it with a parametrization of Mg-Mn partitioning ($K_D{}^{Mg-Mn}_{Ol-melt}$), allowing the estimation of the $F^{3+}/\sum Fe$ of the melt in addition to modelling the PEC process. This model was not applied in the present study as it is not included in the MIMiC program and we did not perform high-precision MnO analyses, which would have been necessary to calculate accurate oxidation conditions.

Corrections for CO_2 contents lost to the bubble are performed by applying a calculated-volume approach to model the vapour-bubble growth that accounts for diffusive limitations of CO_2 addition to the vapour bubble and differential deformation of the melt and host (see details in Rasmussen *et al.*, 2020). Sample dimensions (host, MI, and vapour bubble) or cooling rate estimations are needed for the application of this model. Here, estimated dimensions are used, measured from optical microscope and BSE images of the exposed MIs. Vapour bubbles were assumed to be perfect spheres, MIs and Ol-hosts are assumed to be ellipsoids with the perpendicular dimension to the observed plane having a radius equal to the smallest measured radius in the observed plane. Uncertainties (1σ) on these measurements were estimated as 1.6 vol% of vapour-bubble, 3 μm of MI average diameter, and 10 μm of olivine average diameter. These uncertainties were estimated by performing repeated measurements from the images.

One of the modifications made to the original MIMiC program was the implementation of the H_2O-CO_2 solubility model of Papale *et al.* (2006) in replacement of the VolatileCalc model (Newman & Lowenstern, 2002). This modification was necessary as many of the MI compositions in this study are outside the SiO_2 range of the VolatileCalc parametrization of basaltic compositions (i.e., their SiO_2 content exceeds 52 wt%).

The original H_2O content of the MIs is estimated using the $D_{CaO}^{Ol-melt}$-dependent hygrometer of Gavrilenko *et al.* (2016a). This model is implemented in the MIMiC program by performing iterative calculations of the MI corrections followed by H_2O estimations using the corrected MI compositions and the measured host Ol Ca content. The first iteration uses the measured H_2O content, followed by a second iteration where the H_2O content of the uncorrected composition is updated to the new H_2O estimated value, adjusted by the amount of PEC predicted in the previous correction stage. This process is repeated until the estimated H_2O content converges (usually after three or four iterations). Uncertainties of the H_2O estimations (1σ) are set to 1.1 wt% (Gavrilenko *et al.*, 2016a). Uncertainty estimations of MIMiC results are obtained through Monte Carlo simulation of 50 iterative calculations of each MI correction, applying the defined uncertainties of all input values (melt and olivine compositions, as well as bubble, MI and Ol-host sizes). The modified MIMiC script is provided in the Supplementary Material.

Corrections were first applied without any Fe-loss correction and the corrected compositions were assessed for evidence of 'Fe-loss' indicators. The MIs of each tephra sample with the exception of AKN are hosted in a very narrow range of olivine compositions, whereas their range in oxides, like SiO_2 or K_2O, indicates substantial amounts of differentiation within the MI compositions. This results in a MgO vs FeO_T trend at nearly constant Mg#. The Fe-loss correction displaces MI compositions along a constant Mg# line, making Fe-loss difficult to estimate just by observing the MgO vs FeO_T trends. Figure 6 shows MgO vs FeO_T and SiO_2 vs FeO_T compositions of the uncorrected and corrected MI trend. The size of the symbols in these diagrams are proportional to the size of the MI and the distance between the corrected and uncorrected MIs (marked by the dotted line) is proportional to the calculated PEC amount (wt%). It is seen that there is no clear correlation between FeO_T content and the MI size as there are small MIs with higher FeO_T contents than bigger MIs with similar SiO_2 contents. This indicates that Fe-loss is negligible during PEC triggered by ascent and eruption and that the constant Mg# of the melt (or constant Fo content of the olivine) trends observed in Fig. 6 are product of the re-equilibration of MIs trapped at different stages of melt differentiation to a constant Mg# of the surrounding melt during prolonged storage times (Brahm *et al.*, 2021). As Fe-loss is promoted for slow cooling rates, it can be expected that most Fe-loss occurs through PEC during storage. Since the MIs reached equilibrium before eruption and the PEC

Table 2: Glass composition of the MIs measured with EPMA (in wt%)

Sample	SiO_2	TiO_2	Al_2O_3	FeO_T	MnO	MgO	CaO	Na_2O	K_2O	P_2O_5	Total	Fo[1]
Akita-Komagatake												
AK-135	52.98	1.09	14.83	9.50	0.19	5.27	9.77	2.42	0.30	0.15	96.49	78.0
AK_136	52.54	1.16	16.18	9.47	0.16	2.51	10.48	2.00	0.36	0.19	95.06	78.0
AK-41.1	54.68	1.08	16.78	9.36	0.10	2.43	10.35	2.76	0.34	0.12	98.00	77.4
AK_137b	54.90	1.17	16.97	9.44	0.14	3.40	10.88	2.51	0.33	0.12	99.85	77.4
AK-42.1	53.24	1.10	15.29	10.36	0.14	5.57	9.43	2.46	0.34	0.19	98.12	77.8
AK-38.1	52.75	0.94	15.18	10.21	0.15	5.88	9.59	2.36	0.28	0.14	97.48	78.1
AK-36.1	50.29	0.84	15.73	11.56	0.14	6.57	10.13	2.15	0.22	0.10	97.74	78.3
AK-47.1	51.99	0.96	15.13	10.44	0.15	6.09	9.96	2.26	0.27	0.09	97.35	77.8
AK-143	55.16	1.30	17.25	8.42	0.16	2.12	10.62	2.81	0.40	0.15	98.39	78.1
AK_144	52.12	0.93	15.10	10.93	0.17	5.45	10.00	2.23	0.29	0.11	97.32	77.5
AK-145.2	51.16	0.94	15.28	10.32	0.20	6.19	10.10	2.13	0.22	0.11	96.63	77.5
AK_146	55.44	1.13	16.38	9.96	0.24	3.57	10.45	2.53	0.34	0.15	100.17	77.5
AK_148	54.35	1.12	15.89	9.92	0.17	3.71	10.26	2.28	0.35	0.25	98.28	77.5
AK_149	52.17	1.03	14.93	10.70	0.22	5.42	9.67	2.02	0.30	0.12	96.58	77.5
AK-151	54.35	1.08	15.98	9.33	0.19	4.12	9.46	2.54	0.35	0.14	97.53	77.9
AK-39.1	54.18	1.17	15.87	9.52	0.12	2.82	10.61	2.72	0.35	0.18	97.54	77.7
AK-153	51.44	0.97	15.50	11.05	0.18	6.30	10.07	1.86	0.20	0.13	97.71	78.5
AK-43.1	51.71	0.96	16.12	10.82	0.17	4.20	10.74	2.17	0.24	0.16	97.30	77.5
AK-43-53	54.56	1.12	16.56	9.29	0.14	2.53	10.24	2.74	0.37	0.19	97.72	77.5
Hakkoda												
HK-51	50.60	1.03	15.82	10.57	0.25	4.19	8.57	2.36	0.19	0.17	93.75	71.7
HK_52	50.51	1.01	16.55	11.33	0.18	2.61	9.08	2.27	0.25	0.12	93.90	72.5
HK_54	49.01	0.51	16.29	10.72	0.26	5.38	9.33	1.92	0.17	0.12	93.71	76.7
HK-30.1	50.35	0.95	18.65	9.83	0.14	2.73	10.64	2.38	0.21	0.12	96.00	77.0
HK-23.1	49.53	0.89	16.84	11.46	0.17	5.17	9.89	2.07	0.17	0.10	96.28	76.8
HK_57	49.00	0.86	15.91	11.12	0.19	5.40	9.66	1.69	0.15	0.09	94.07	76.4
HK_58	49.69	0.84	16.33	11.16	0.18	5.17	9.74	1.78	0.17	0.12	95.17	77.1
HK_59	51.63	1.11	17.63	11.05	0.21	2.58	9.22	2.50	0.29	0.13	96.34	72.6
HK_60	50.74	0.91	18.19	9.48	0.20	3.51	10.14	2.04	0.21	0.06	95.47	78.1
HK_61	49.36	0.80	16.39	11.14	0.17	5.05	9.45	1.75	0.20	0.09	94.38	77.0
HK_62	51.88	1.09	16.98	11.52	0.19	2.84	8.93	2.62	0.27	0.13	96.46	72.0
HK-34.1	49.57	0.83	15.99	10.78	0.13	6.18	9.45	1.94	0.17	0.13	95.16	76.7
HK-64	51.35	0.92	18.09	9.71	0.21	3.35	9.39	2.29	0.22	0.11	95.63	77.7
Tokachidake												
TK_01	46.08	1.11	18.17	9.58	0.16	5.02	11.56	2.53	0.59	0.23	95.03	76.9
TK_02	48.51	1.18	19.22	9.94	0.21	3.51	11.90	2.19	0.54	0.25	97.45	76.9
TK_03	48.42	1.16	21.07	7.46	0.16	2.09	12.08	2.76	0.61	0.20	96.01	76.8
TK-04	46.46	1.06	17.91	10.97	0.24	5.43	10.84	2.03	0.53	0.18	95.65	77.3
TK_06	48.04	1.17	19.73	8.65	0.18	2.75	11.72	2.76	0.55	0.23	95.76	77.1
TK-07	46.68	1.07	18.54	10.39	0.22	4.56	11.63	2.59	0.59	0.20	96.49	76.8
TK-08	46.75	1.11	18.55	10.81	0.19	3.86	11.97	2.48	0.63	0.24	96.58	76.8
TK_09	48.07	1.14	19.29	9.71	0.19	2.96	11.84	2.34	0.61	0.23	96.38	76.8
TK-10	47.21	1.13	19.05	9.87	0.19	3.59	11.52	2.73	0.59	0.22	96.11	76.8
TK_11	49.98	1.11	20.03	8.64	0.14	2.16	10.44	2.89	0.91	0.28	96.57	74.8
TK-12	47.63	1.04	18.64	10.25	0.18	3.80	11.64	2.73	0.57	0.15	96.64	76.6
TK_13	48.00	1.15	19.60	8.88	0.21	2.48	11.93	2.70	0.60	0.18	95.73	77.0
TK-14	46.99	1.04	18.77	9.80	0.20	5.15	10.88	2.35	0.61	0.17	95.97	76.8
TK_15	47.56	1.06	18.60	9.80	0.18	3.66	11.82	2.39	0.50	0.20	95.77	76.8
TK-16	51.10	1.44	16.98	10.41	0.22	4.44	8.59	2.34	1.14	0.19	96.85	74.0
TK-17	47.35	1.16	19.07	9.84	0.19	3.70	11.88	2.59	0.56	0.19	96.54	76.7
TK-18	47.71	1.07	18.74	10.43	0.20	3.91	11.41	2.56	0.55	0.27	96.85	76.8
TK-19	48.60	1.08	19.16	9.49	0.18	2.67	11.76	2.70	0.58	0.21	96.42	76.9
TK_23	48.47	1.04	17.60	10.66	0.19	4.93	9.95	2.58	0.75	0.21	96.36	75.3
TK_24	49.18	1.48	19.60	9.30	0.15	2.23	11.06	2.24	0.83	0.25	96.30	75.3

(Continued)

Table 2: Continued

Sample	SiO_2	TiO_2	Al_2O_3	FeO_T	MnO	MgO	CaO	Na_2O	K_2O	P_2O_5	Total	Fo[1]
Akan-fuji												
AKN_95	47.05	0.88	16.89	12.18	0.22	4.90	10.59	1.94	0.36	0.06	95.05	74.9
AKN_100	48.00	0.86	18.12	10.46	0.19	5.06	11.11	2.07	0.50	0.08	96.44	79.9
AKN_101	48.41	0.94	15.60	13.68	0.30	4.98	9.78	1.99	0.42	0.17	96.26	73.4
AKN_102a	48.81	0.99	16.59	12.27	0.21	3.21	10.50	2.18	0.50	0.26	95.52	73.4
AKN_112	48.23	0.90	16.48	13.20	0.18	3.93	10.37	2.01	0.50	0.11	95.92	72.4
AKN-117	49.72	0.91	15.72	11.81	0.18	5.07	9.19	2.27	0.65	0.07	95.60	73.1
AKN_118	48.42	0.99	16.61	12.50	0.23	3.73	10.22	2.19	0.47	0.14	95.49	73.1
AKN_123	49.30	0.88	17.41	10.68	0.23	4.41	10.30	2.06	0.62	0.12	95.99	78.4
AKN_124	47.57	0.74	16.32	12.78	0.23	5.16	9.70	1.82	0.46	0.07	94.85	73.9
AKN-94	49.96	0.89	16.54	12.49	0.20	3.57	10.66	2.15	0.60	0.14	97.21	71.8
AKN_97	53.19	1.39	13.68	14.58	0.26	2.28	7.58	2.49	1.04	0.20	96.68	61.8
AKN-99	52.00	0.80	15.96	11.63	0.22	5.17	8.95	2.25	0.74	0.12	97.83	74.4
AKN-105	54.04	1.08	14.57	10.76	0.20	4.75	8.74	2.18	0.82	0.09	97.23	75.1
AKN_106	50.36	0.96	15.66	11.50	0.27	5.19	10.06	2.11	0.62	0.09	96.82	77.1
AKN-116	51.45	0.94	15.52	11.38	0.18	5.16	9.50	2.31	0.58	0.14	97.15	75.8
AKN_122	50.99	0.96	14.93	11.06	0.17	5.17	10.08	1.83	0.56	0.10	95.84	74.9
AKN_132c	51.03	0.98	16.08	12.68	0.24	4.39	10.67	2.36	0.60	0.10	99.13	74.5
AKN_108	47.33	0.85	17.94	10.69	0.19	5.61	11.39	1.90	0.37	0.09	96.36	80.1
AKN_120	45.13	0.84	18.78	9.94	0.14	5.46	12.42	1.71	0.24	0.08	94.74	81.6
AKN_130a	46.69	0.85	16.39	13.58	0.22	4.75	12.03	1.50	0.27	0.05	96.33	74.5
AKN_130b	46.84	0.78	16.58	13.31	0.19	5.04	11.63	1.79	0.31	0.11	96.57	74.5
AKN_130c	47.04	0.87	17.24	13.03	0.23	3.54	12.47	1.78	0.28	0.06	96.54	74.5
AKN_130d	46.30	0.86	16.87	12.49	0.25	4.02	12.33	1.59	0.29	0.09	95.09	74.5
AKN_130e	46.37	0.82	16.50	13.05	0.23	4.74	11.69	1.52	0.31	0.06	95.30	74.5
AKN-131a	46.86	0.86	17.37	12.44	0.20	3.74	12.21	2.01	0.28		95.98	74.5
AKN-132a	46.56	0.79	17.09	12.43	0.25	4.38	11.95	1.72	0.28	0.06	95.51	74.5
AKN_134b	47.20	0.88	18.18	12.16	0.25	3.43	12.21	1.56	0.31	0.07	96.25	74.5
Tya-Tya												
TT-67.10	50.62	1.13	16.11	12.86	0.18	3.71	9.22	2.89	0.62	0.21	97.53	71.6
TT-67.2	52.45	1.22	15.70	12.49	0.19	3.84	8.74	2.98	0.80	0.16	98.58	70.9
TT-68.1	50.44	1.04	15.46	12.42	0.17	4.52	8.87	2.61	0.58	0.19	96.29	71.1
TT-68-75	51.88	1.13	15.52	11.75	0.18	4.20	8.87	2.99	0.61	0.20	97.32	71.1
TT-68-76	50.99	1.18	17.08	12.17	0.20	2.80	9.79	2.91	0.64	0.21	97.97	71.1
TT-71	50.61	1.10	16.13	12.36	0.23	4.17	9.02	2.67	0.54	0.19	97.02	71.9
TT-72	50.13	1.07	15.51	11.17	0.19	4.91	8.82	2.55	0.52	0.25	95.10	72.3
TT-73.2	50.49	1.12	15.61	11.13	0.24	4.44	8.93	2.71	0.49	0.20	95.36	72.3
TT-74	51.27	1.17	16.58	11.62	0.23	3.23	9.32	2.90	0.51	0.24	97.06	72.3
TT-75	51.23	1.12	16.47	11.73	0.22	4.25	9.17	2.60	0.53	0.16	97.47	71.8
TT_76	50.73	1.16	16.60	11.58	0.21	3.50	9.11	2.69	0.65	0.21	96.45	71.8
TT_77	50.26	1.08	15.87	12.20	0.21	4.35	8.98	2.62	0.60	0.17	96.32	71.8
TT-78	50.28	1.07	15.79	11.46	0.26	4.50	8.78	2.78	0.58	0.16	95.67	71.8
TT-79	51.50	1.21	17.46	10.17	0.18	2.07	9.63	3.03	0.62	0.17	96.05	72.8
TT-80	50.19	1.17	16.97	11.95	0.25	3.87	9.73	2.91	0.56	0.25	97.85	72.1
TT-81	50.36	1.11	16.63	12.21	0.23	3.91	9.52	2.85	0.53	0.20	97.55	72.1
TT-82	50.68	1.18	16.08	11.40	0.26	3.31	9.31	2.55	0.56	0.24	95.57	72.2
TT_83	53.17	1.27	16.99	10.09	0.19	2.39	9.35	2.82	0.71	0.19	97.16	72.2
TT-85	50.87	1.12	15.83	11.41	0.23	3.89	9.13	2.59	0.52	0.21	95.79	72.3
TT-86	50.07	1.09	15.73	12.66	0.26	3.90	9.26	2.59	0.54	0.20	96.31	72.3
TT-89	50.60	1.14	16.39	12.34	0.20	4.39	8.92	2.74	0.60	0.20	97.52	71.9
TT_90	49.00	1.26	17.59	11.20	0.20	2.35	9.65	2.74	0.70	0.24	94.92	71.3
TT_91	50.83	1.04	16.30	11.42	0.21	3.62	9.04	2.15	0.62	0.19	95.42	72.0
TT-66.1	50.99	1.07	15.57	11.64	0.18	4.70	8.75	2.61	0.61	0.20	96.29	71.4
TT_92b	51.85	1.10	15.74	11.47	0.25	3.71	8.65	2.60	0.69	0.20	96.23	71.4
TT-65.1	50.60	1.11	19.13	9.33	0.13	2.17	10.75	2.99	0.48	0.20	96.88	75.0

[1]Forsterite content of olivine host.

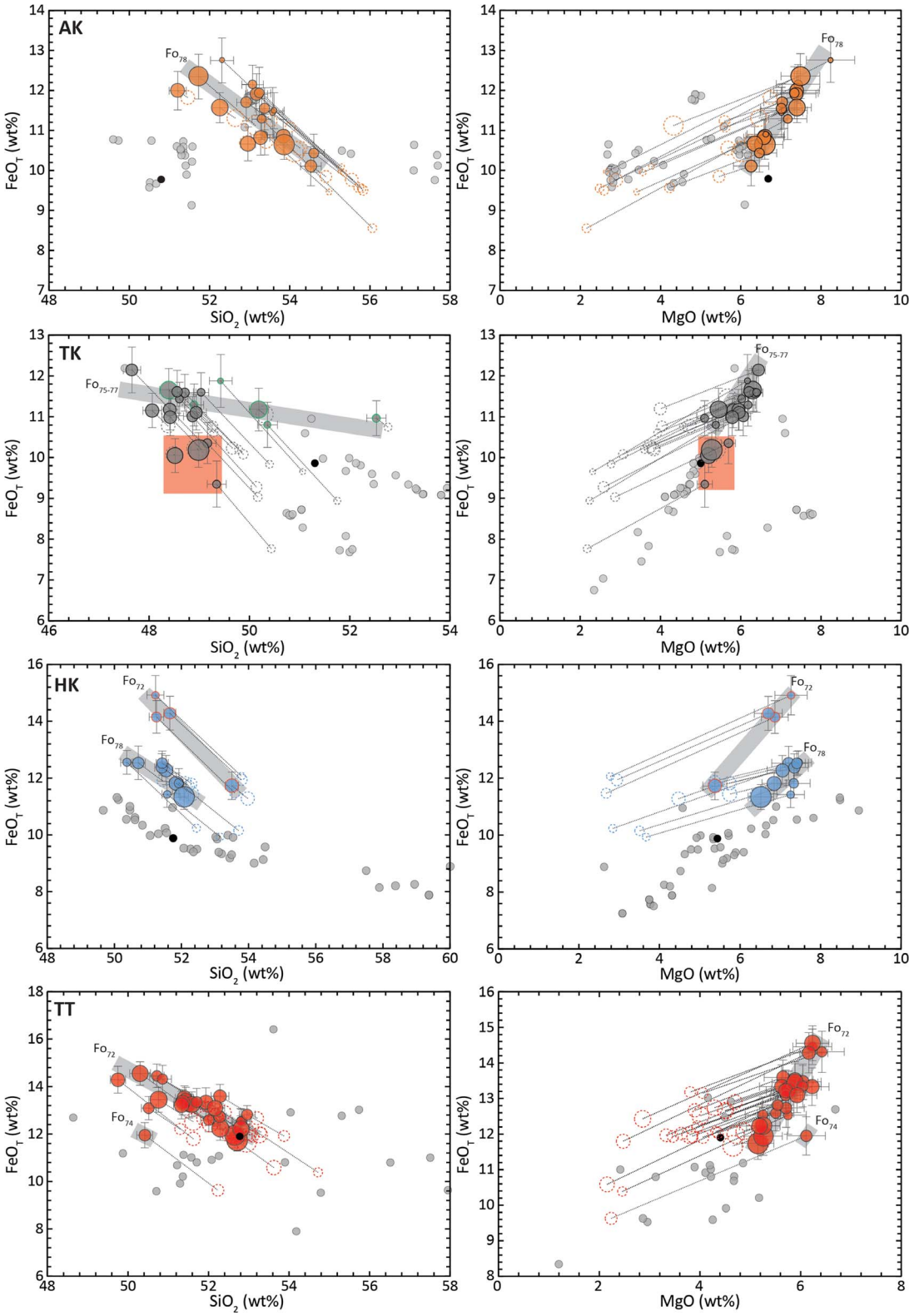

Figure 6 Variation diagrams of PEC-corrected MI compositions calculated with the MIMiC program. Filled circles correspond to the corrected MI compositions, hollow circles correspond to the uncorrected MI compositions. Black small circle is the whole rock composition of each tephra sample and grey small circles are whole rock data from the literature. The size of the circles is proportional to the size of the MIs. The dotted black lines connect the corrected and un-corrected MI compositions, and the length is proportional to the amount of PEC. The grey bands indicate the trends of different populations of MIs defined by the compositions of their Ol hosts. The filled circles with green outlines in the TK sample indicate the MIs that do not present daughter crystals and the red area indicates the MI compositions strongly affected by crystallization of daughter crystals. Error bars correspond to 1σ. Uncorrected MIs errors are smaller than symbol size.

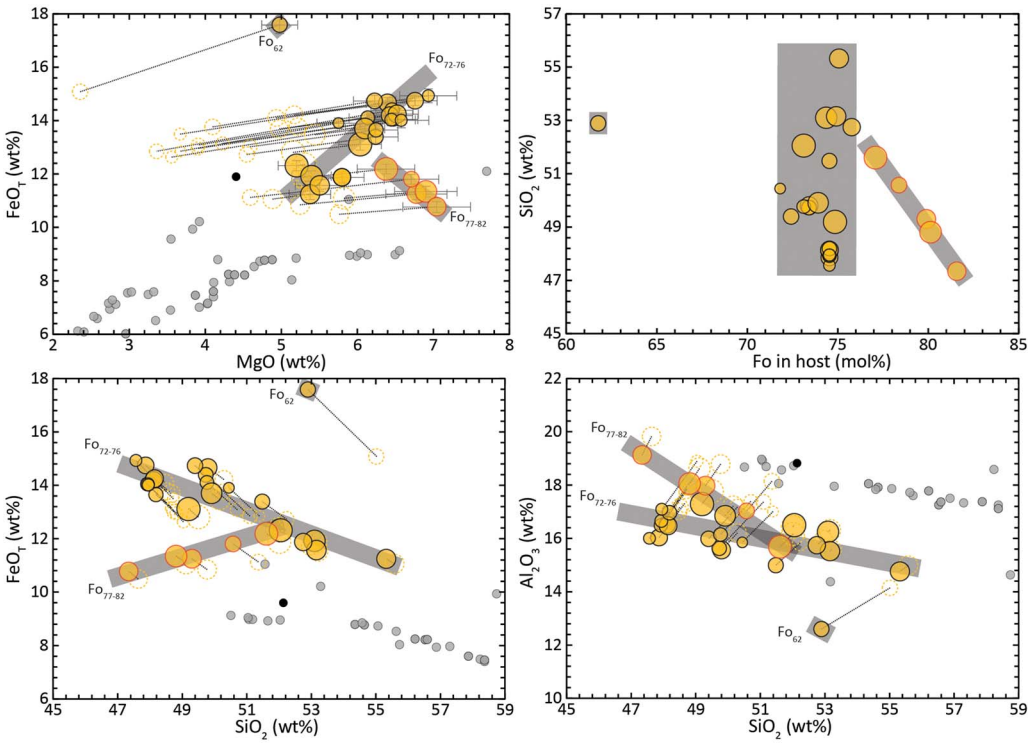

Figure 7 Variation diagrams of PEC-corrected MI compositions of the AKN sample calculated with the MIMiC program. Symbols are the same as Fig. 6. Error bars correspond to 1σ. Uncorrected MIs errors are smaller than symbol size.

triggered during ascent and eruption of tephras is typically fast (0.1–3 m/s; compilation in Browne & Szramek, 2015), it is expected that MIs show little to no evidence for Fe-loss. All PEC-corrected MI compositions are available in the Supplementary Material.

Akita-Komagatake. All MIs from AK belong to the same Fo group (Fo$_{\sim 78}$) and appear to follow the same FeO$_T$ vs SiO$_2$ trend.

Hakkoda. In the corrected MI from HK (Fig. 6) two trends can be distinguished with distinct FeO$_T$ concentrations. These trends distinguish two distinct compositional Ol populations (Fo$_{\sim 72}$ and Fo$_{\sim 78}$).

Tya-Tya. In the TT sample, the MI hosted in an outlier Ol of Fo$_{74}$ (interpreted as a xenocryst) can be distinguished from the main trend of constant Fo$_{72}$.

Tokachidake. The trend followed by the MIs with no evidence of formation of daughter crystals is shown in the variation diagrams of TK in Fig. 6. The MIs with some evidence of crystallization of daughter crystals that closely follow the same trend are interpreted as having a negligible effect of fractionation of daughter crystals. The amplitude of this effect is dependent not only on the amount of crystallization but also on the location of the analysis spot and the amount of diffusion that occurred in the melt after the crystallization of these daughter crystals. There is a group of four MIs that are depleted in Fe and Mg with respect to the trend that the rest of the MIs in TK. These MIs have a high proportion of Px daughter crystals relative to their MI volume, thus have been the most affected by this crystallization, and therefore are excluded from further analysis.

Akan-fuji. The analysis of the AKN MIs is more complex. From the petrography of the tephras, it is clear that there must have been mingling (and probably mixing) between two magma batches before eruption, generating two distinct tephra types. The Ol compositional range is very wide in comparison with the other samples and at first glance it is hard to distinguish the provenance of the Ol crystals from the two magma batches. PEC-corrected MI compositions (Fig. 7) show two distinct behaviours. A clear correlation between SiO$_2$ increase with Fo decrease is observed for MIs in Ol hosts of Fo$_{76–82}$, which also follow an increasing trend in FeO$_T$ with SiO$_2$ and a decreasing trend of MgO and Al$_2$O$_3$. This differentiation path is compatible with fractionation of an Ol + Pl (± Px) assemblage. A contrasting behaviour is observed for the MIs hosted in Ol hosts of Fo$_{72–75}$, where there is no correlation of Fo content with SiO$_2$, but there is a decrease of FeO$_T$ and MgO with SiO$_2$, and the Al$_2$O$_3$ decrease is less steep than in the other MI group. Here, the latter MI group is interpreted as hosted in long-stored Ol crystals, which have reached equilibrium with the stored melt, whereas the former MI group is interpreted as recently trapped MIs from Ol crystals coming with the new magma batch. The outlier MI is hosted in an Ol of Fo$_{62}$, which is interpreted as a picked-up xenocryst.

Figure 8A shows the estimated H$_2$O-CO$_2$ compositions of the MIs with the measured concentrations for comparison. The substantially higher H$_2$O contents predicted by the hygrometer indicate that significant dehydration occurred to all MIs. Dehydration could have occurred during ascent and eruption by diffusive loss of H$^+$, as it has been shown that timescales of H$^+$ diffusion in Ol are faster than for any other element (Hartley *et al.*, 2015; Turner *et al.*, 2017a). Corrected H$_2$O compositions range from *c.* 3.4 wt% to *c.* 7.4 wt%. The AK sample has the lowest H$_2$O concentrations (*c.* 3.4 wt% to *c.* 5.2 wt% H$_2$O), followed by AKN, HK, and TT that overlap in H$_2$O concentrations (from *c.* 4.4 to *c.* 6.2 wt% H$_2$O, with one HK outlier of *c.* 6.8 wt%). The TK sample H$_2$O estimations are the highest (*c.* 6.2 wt% to *c.* 7.4 wt% H$_2$O). Corrected CO$_2$ compositions are <500 ppm for most MIs in all samples, with some higher concentrations (<1000 ppm) for some MIs of HK and TT.

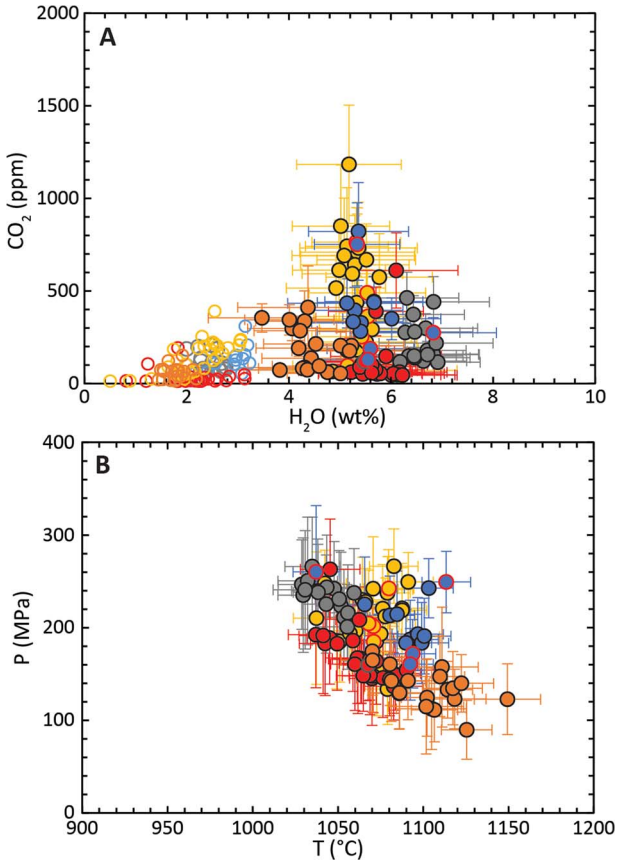

Figure 8 (A) Measured (hollow circles) and corrected (filled circles) volatile contents and (B) estimated P–T storage conditions for all MIs. Corrected compositions and P–T conditions were calculated with the MIMiC program and the Ol-melt hygrometer. Colour scheme is the same than Fig. 1. Error bars correspond to 1σ.

AKN shows the highest variability in CO_2 estimations, with about half of the MIs having concentrations in the range of 500–1000 ppm and an outlier of *c.* 1200 ppm.

Thermobarometry

The corrected major and volatile elements contents of the MIs provide estimations of equilibrium temperature (Ol-melt thermometer of Putirka *et al.*, 2007) and H_2O-CO_2 saturation pressures (Papale *et al.*, 2006) (Fig. 8B). Pressure estimations indicate that the magmas were stored at variable depths in the upper crust (*c.* 100–300 MPa) at temperatures of *c.* 1030–1150°C. The P–T correlation observed here, with hotter melts stored at higher depths, arises from the pressure control on H_2O solubility. As these are saturation pressures, saturation needs to be assumed to interpret them as storage pressures. Saturation can be safely assumed for most MIs as corrected CO_2 concentrations are low. High-H_2O melts are then stored at higher depths and are colder because of the effect that H_2O has on depressing the liquidus temperature of silicate melts. Zellmer *et al.* (2016) proposed that high-H_2O and low-T melts stall at deeper levels due to early degassing-driven crystallization, whereas low-H_2O and high-T melts have a higher ascent potential due to their late degassing.

Available Cpx-Opx pairs from the AKN and HK samples where used to estimate temperatures, employing the two-pyroxene thermometer of Putirka & Tepley, (2008) (equation 36). Three temperatures calculated for the AKN sample give 1041°C–1054°C (±56°C), which overlaps with the 1037°C–1095°C range of the Ol-melt thermometry. Twenty-eight Px pair temperatures from the HK sample yield a 1003°C–1089°C (±56°C) range, also overlapping with the 1037°C–1113°C range yielded by the corrected MIs.

Assessing the differentiation process of the MI trends

Testing homogeneous fractional crystallization using MushPEC

As discussed above, most MI populations show evidence of being completely re-equilibrated with the interstitial melt during storage. An attempt to estimate MI compositions at entrapment was done using the MushPEC program (Brahm *et al.*, 2021). This method finds the best fit of a MI set to a liquid line of decent produced by HFC models generated with the rhyolite-MELTS algorithm (Ghiorso & Sack, 1995; Gualda *et al.*, 2012). It does so by adjusting the Ol amount added/subtracted and Fe-Mg exchange with the Ol host. Iterative HFC models are generated by varying five initial parameters: (1) Ol addition/subtraction, (2) Fe/Mg ratio of the initial MI composition, (3) initial H_2O content, (4) pressure, and (5) f_{O_2} conditions. The fit is found by minimizing the Aitchison distance (Aitchison, 1986) between the corrected MIs and the liquid line of decent of the HFC models. The fitted composition consists in the following major oxides in mol% units: SiO_2, Al_2O_3, $FeO_T + MgO$, CaO, and K_2O.

Figures 9–13 show the best fit models produced by MushPEC for each of the samples in variation diagrams of Al_2O_3, TiO_2, Na_2O, and P_2O_5. These diagrams are in mol% units with K_2O on the abscissa. The fitting of the major oxides associated with the major mineral phases involved during crystallization of basaltic melts (Ol, Pl, and Px) is here represented just by the Al_2O_3 variation diagram. It is important to note that these diagrams are insensitive to the composition of the olivine during PEC corrections and have low sensitivity to the amount of PEC, as are incompatible elements during olivine fractionation with slow diffusivities. MushPEC is able to find good fits for these major oxides that represent the probable HFC trends that the MIs may have followed at entrapment. However, the other three minor elements have significant discrepancies, which are associated to the involvement of Ti-Mag (TiO_2) and apatite (P_2O_5) accessory phases and the composition of Pl. With the exception of AK, all samples show a sub-horizontal TiO_2 trend, which indicates that some Fe-Ti oxide phase (probably Ti-Mag) must have been involved during fractionation. All HFC models produced by MushPEC show a conservative behaviour of TiO_2 until Ti-Mag enters the fractionation sequence, generating a sharp change in the trends where TiO_2 starts to decrease strongly during differentiation. Decrease of TiO_2 with differentiation can also be caused by fractionation of amphibole (e.g., Molina *et al.*, 2009; Liao *et al.*, 2021); however, there is no evidence of amphibole crystallization in any of these samples. A similar behaviour to TiO_2 is observed for Na_2O in the TT and AKN samples and for P_2O_5 in the TK and TT samples. Sub-horizontal trends in the P_2O_5 variation diagrams indicate the involvement of apatite (P_2O_5), which is not observed in the samples and furthermore is not expected to be equilibrated in these melt compositions. The flat Na_2O trends indicate the involvement of a Pl phase with compositions of higher albite content than the ones in equilibrium with the basic melt.

The AK MIs appear to better fit the HFC trends, showing an upward trend in all three minor oxides, but with the TiO_2 trend of the MIs following a slightly lower sloped trend than the HFC models. This sample was actually previously used by (Brahm *et al.*, 2021) to validate the MushPEC program. Nonetheless, strong discrepancies

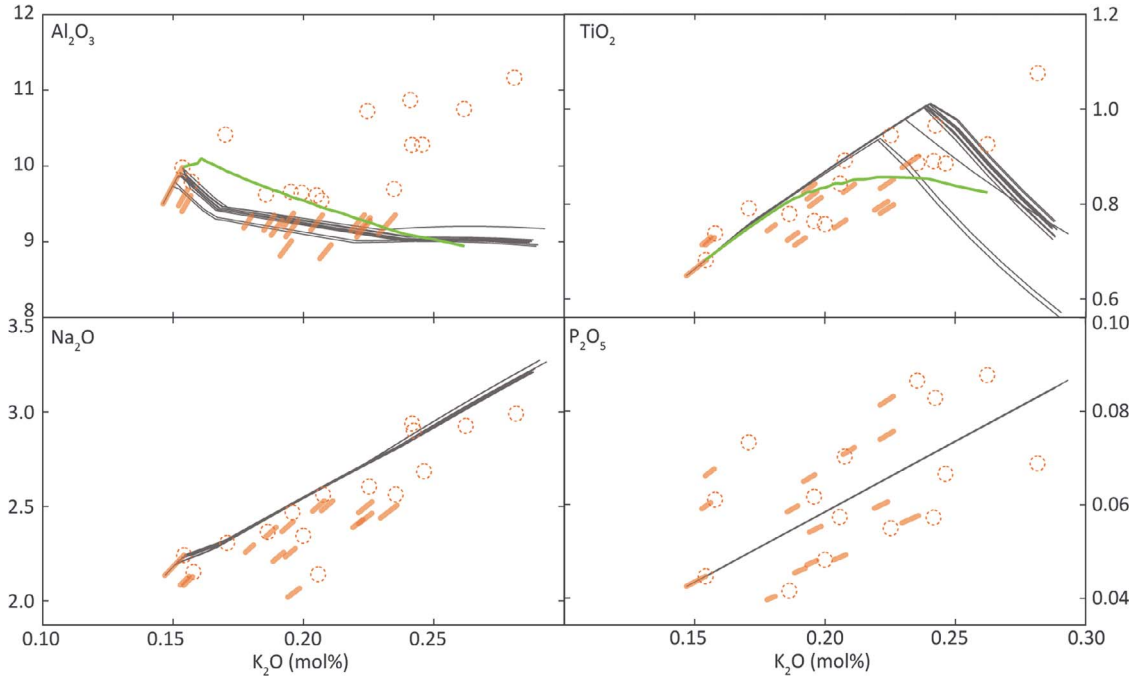

Figure 9 Variation diagrams showing the MushPEC results for the AK sample. Dashed circles are the uncorrected MI compositions, the coloured lines indicate the ranges of compositions for the MIs corrected by MushPEC assuming that the MIs follow a HFC differentiation path. Black lines correspond to the best fit HFC models calculated with rhyolite-MELTS for the MI set. Green line indicates the BLF model example (see Discussion). Uncertainties (1σ) of the measured MI compositions are smaller than the symbol size.

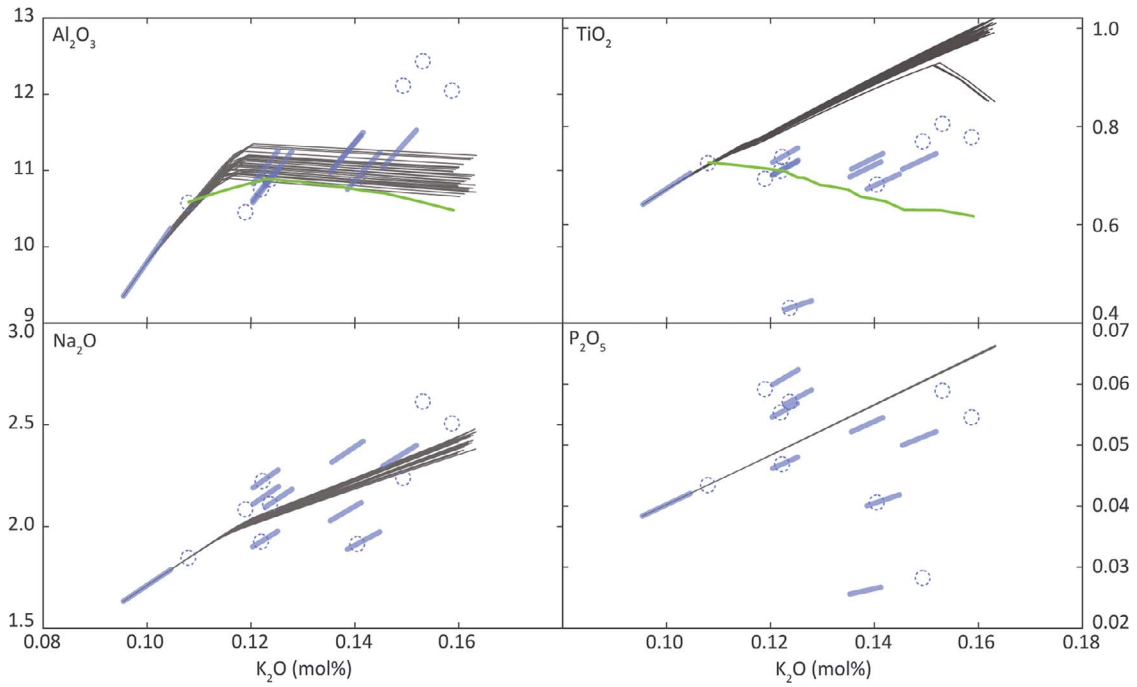

Figure 10 Variation diagrams showing the MushPEC results for the HK sample. Figure description as in Fig. 9. Uncertainties (1σ) of the measured MI compositions are smaller than the symbol size.

appear between the H_2O contents of the MIs estimated in this study and the ones predicted with MushPEC.

In addition to the estimated initial MI compositions, MushPEC also provides estimations on the crystallization conditions. Table 3 shows the estimated H_2O and P range for the corrected MI populations with MushPEC and the estimations made applying the PEC corrections with MIMiC and the Ol-melt hygrometer. It is seen that all H_2O contents estimated using the Ol-melt hygrometer

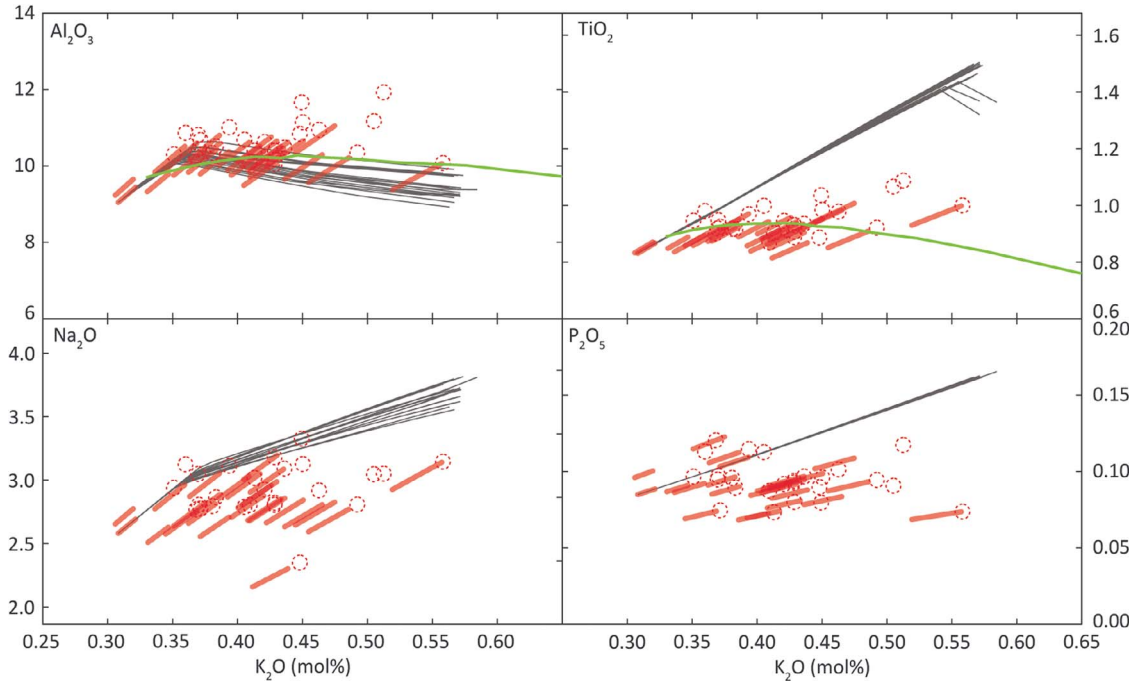

Figure 11 Variation diagrams showing the MushPEC results for the TK sample. Figure description as in Fig. 9. Uncertainties (1σ) of the measured MI compositions are smaller than the symbol size.

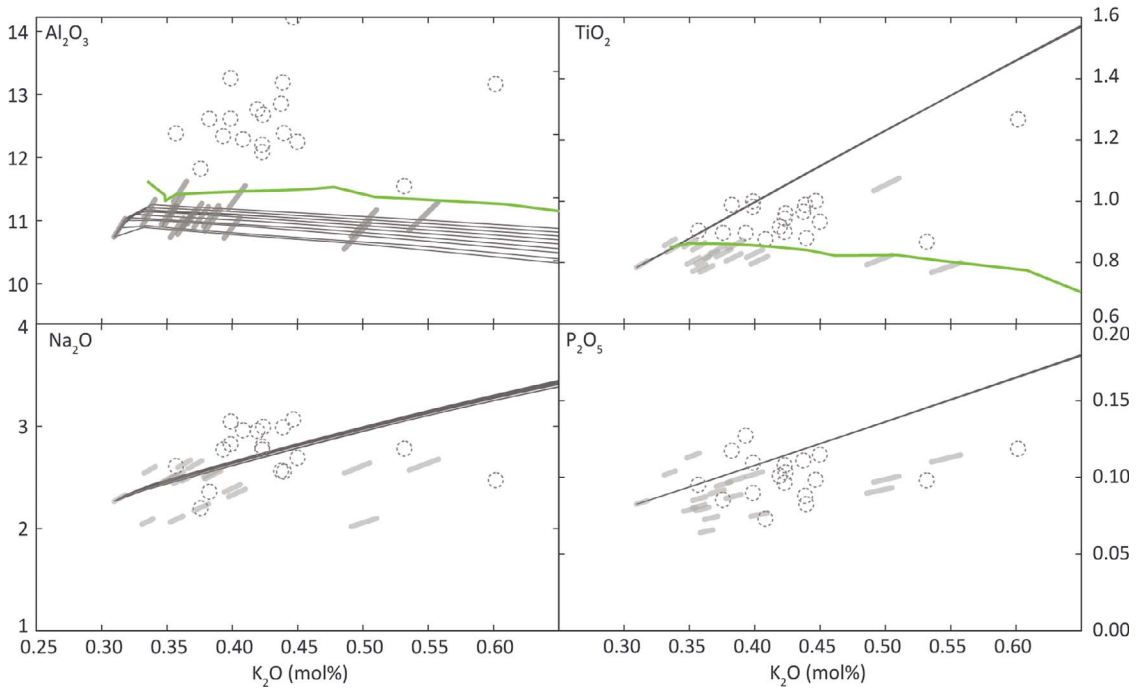

Figure 12 Variation diagrams showing the MushPEC results for the AKN sample. Figure description as in Fig. 9. Uncertainties (1σ) of the measured MI compositions are smaller than the symbol size.

are significantly higher than the ones determined through MushPEC, where the latter yields undersaturated conditions at the predicted pressures (Table 3). These discrepancies also include the AK sample.

The inability of MushPEC to reproduce the differentiation trends indicates that the mechanism of melt differentiation cannot be assigned as simple HFC. The process of HFC produces clear 'kinks' or breaks in variation diagrams associated with the entrance or exit of a mineral phase to the crystallization assemblage.

Other pre- and post-entrapment processes

Alternative explanations for the discrepancies between the MI trends and the fitted HFC models involve some pre- and post-entrapment

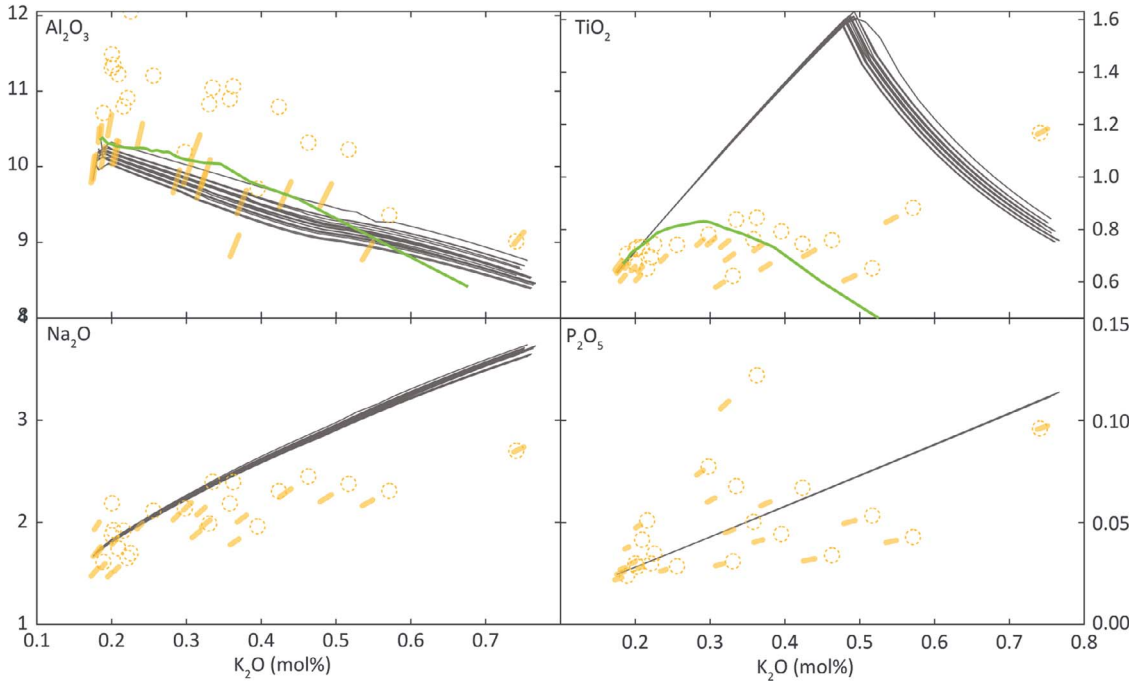

Figure 13 Variation diagrams showing the MushPEC results for the TT sample. Figure description as in Fig. 9. Uncertainties (1σ) of the measured MI compositions are smaller than the symbol size.

Table 3: Estimated H_2O and P range of the MIs from the MushPEC results and from the PEC corrections applied with MIMiC and Ol-melt hygrometry

	MushPEC		MIMiC	
Sample	H_2O (wt%)	P (MPa)	H_2O (wt%)	P (MPa)
AK	1.3–2.2	100–150	3.5–5.2	90–175
HK	2.1–3.7	400	5.1–6.0	160–260
TK	0.5–0.9	300–400	6.2–7.4	200–265
AKN	0.7–1.8	300	4.4–6.1	115–275
TT	0.5–1.3	300–400	5.1–6.2	135–275

processes. For example, Danyushevsky *et al.* (2004) identified populations of olivine-hosted MIs with unusual major and trace element compositions, which showed high variability and discrepancies with the carrier melt. All these populations were found to be Fo-rich (>85 mol%) and were interpreted as localized, grain-scale dissolution–reaction–mixing processes that captured localized melt heterogeneities not representative of the main magma evolution. These characteristics were not observed in MIs from Fo-poorer olivine hosts, as such reactions relate to early stages of magmatic evolution. It is then unlikely that these processes affected the composition of the MIs in this study (<80 mol% Fo). Hence, the compositional variations observed within each MI group, once post-entrapment processes are assessed, should reflect the evolution of the main melt and not just localized processes.

Recently developed models of post-entrapment processes propose other mechanisms to introduce compositional variations of olivine-hosted MIs. Newcombe *et al.* (2014) found that compositional variations can arise from contrasting diffusivities of major components within MIs. Compositional profiles in MIs develop through PEC during ascent and eruption. The short times from PEC to quenching (seconds to hours) preserve these profiles which undergo only partial diffusion. The compositional profile of fast diffusing elements (e.g., Ca) relaxes (homogenizes) faster than of slow diffusing elements (e.g., Al). This generates an increase in major oxide ratios such as CaO/Al_2O_3 of the glass towards the rims of the MI, as both oxides are enriched towards the MI boundaries, but the CaO profile relaxes faster than Al_2O_3. To avoid most of this compositional variability, the MIs were analysed as close to the centre as possible (although sometimes this was not possible due to the presence of shrinkage bubbles).

As diffusion progresses, fast diffusing elements incompatible in olivine are enriched with respect to incompatible slow diffusing elements towards the centre of the MI until the diffusion rates converge because of the faster relaxation of the profile of the fast-diffusing element. The maximum CaO/Al_2O_3 increase in the centre of the MI is dependent on the amount of PEC and the volume of the MI. If the effect of fast diffusing element enrichment is significant enough to strongly affect the MI compositions, a correlation should be identified between the size or estimated PEC of the MI and the measured CaO/Al_2O_3 ratios. In our samples, however, there is no correlation between the size or PEC amount with CaO/Al_2O_3 ratios (see Supplementary Material). We conclude that compositional variations caused by melt interdiffusion during ascent are not significant compared with the variations between MIs caused by magmatic differentiation.

Further, Portnyagin *et al.* (2019) proposed that H diffusive loss of MIs through the olivine also generates Si diffusive loss out of the MI, producing normative silica-undersaturated MIs in rocks with normative silica-saturated compositions. The possibility of this process affecting the modelled LLDs in how they could reproduce the MI trends is explored in the Supplementary Material. The model of Portnyagin *et al.* (2019) is used to estimate the amount of SiO_2 lost due to MI dehydration by comparing the measured H_2O with

the H_2O content estimated through the Ca-in-olivine hygrometer. Results show that the LLDs produced from melts with higher SiO_2, have the same problem reproducing the trends of minor oxides and overall LLDs are similar to the ones observed in Figs 9–13, displaced towards higher SiO_2 contents and with small effects in the P-H_2O estimations (see Supplementary Material). In addition, most of the best-fit models of these higher SiO_2 runs do not fractionate Ol, indicating that the MIs in our samples cannot have lost much SiO_2 through diffusion, as this would result in the original MI compositions being in disequilibrium with Ol.

Assessing mixing of melts with contrasting compositions to produce the MI trends

As early fractionation of Ti-Mag is expected to produce strong depletion of TiO_2 during differentiation, the sub-horizontal to shallow slopes in most TiO_2 trends may indicate mixing of melts of contrasting compositions, e.g., generated by the interaction of two contrasting magmas during injection of a new magma batch (usually hotter and more primitive) into an evolved magma pocket.

The felsic mixing endmembers that generated the MIs of each of the samples should be relatively high in silica to have fractionated Ti-Mag, apatite, and/or Na-rich plagioclase to generate the observed low slope TiO_2, P_2O_5, and Na_2O trends. Magma mixing of two compositionally contrasting melts should produce strong disequilibrium textures in the phenocrysts. Further, if a mixing event was responsible for the MI trends, it would have to be an old event that was followed by enough time to completely re-equilibrate the Ol host compositions, rather than being related to any evidence of mixing occurring before eruption (e.g., as in the AKN sample).

Irrespective of the time since a presumed mixing event, Pl phenocrysts would preserve records of such magma interactions, as Ca–Na zonation patterns are preserved in this mineral phase. The Pl populations of the five samples include a very common pattern of wide high-An cores with oscillatory zoning within a narrow compositional range (*c.* 10%–15% variation in An content). These perturbations can be generated by temperature perturbances or slight compositional perturbances (particularly H_2O variations), which can be due to convection or thermal interaction with another melt. Mixing of the basic melt with a silica-rich magma would trigger crystallization of Pl growth zones richer in Na within the phenocrysts of the basic melt, but such Na-rich zones are not observed here (cf. Fig. 2).

In addition, several studies about the mechanics of mixing state that high viscosity and density contrasts between the interacting melts hinder the progress of mixing (Sparks & Marshall, 1986; Blake & Fink, 1987; Frost & Mahood, 1987; Sato & Sato, 2009). Thermal homogenization should occur before chemical homogenization as thermal diffusion is faster than chemical diffusion (Sparks & Marshall, 1986). This means that it is highly probable that Ol crystallization is enhanced before any chemical mixing occurs and the trapped MIs should (at least in part) follow a HFC path.

BLF to produce the MI trends

Another process that can reproduce trends similar to mixing is BLF, which can be understood as incremental steps of mixing between the main melt body with marginal amounts of differentiated liquids extracted from the highly crystallized boundary layers (Langmuir, 1989; Nielsen & DeLong, 1992). The fact that the liquids are incorporated in small proportions during magma differentiation makes it feasible for them to be assimilated by the mafic melt, in contrast to what is expected for the interaction of two magma batches of contrasting composition and temperature (Frost & Mahood, 1987).

The observed discrepancies of H_2O estimations (Table 3) can also be explained by invoking BLF. Is it known that H_2O has the effect of depressing the liquidus temperature of silicate mineral phases (Sisson & Grove, 1993; Danyushevsky, 2001; Almeev *et al.*, 2007), but it has a stronger effect in the liquidus depression of Pl (Médard & Grove, 2008; Almeev *et al.*, 2012; Waters & Lange, 2015). This means that H_2O increase produces a delay of plagioclase crystallization with respect to other silicate phases (e.g., Ol and Px). Figure 14A illustrates the behaviour of the HFC paths for different water contents, reflected in an Al_2O_3 variation diagram. Higher H_2O contents delay Pl appearance in the crystallization assemblage, concentrating Al_2O_3 in the melt until Pl begins to fractionate, starting Al_2O_3 depletion. For low H_2O contents, the decrease in Al_2O_3 starts earlier, producing lower concentrations of this oxide in less differentiated compositions. Parman *et al.* (2011) used this behaviour to infer H_2O contents of magmas along the Mariana Arc using the fractionation paths related to the delay of plagioclase crystallization. The decreasing Al_2O_3 trend at low H_2O contents is similar to a mixing line produced by the mixing of the high H_2O melt with the differentiated composition of the same liquid line of decent, and this is how the BLF process is usually modelled (Nielsen & DeLong, 1992). This means that the trend of decreasing Al_2O_3 can be reproduced by a low-H_2O melt with HFC, where Pl appears early in the crystallization assemblage, but it can also be reproduced by BLF of a high-H_2O melt, where Pl is being fractionated in the boundary layer and the central magma body is still above the Pl liquidus temperature. As the H_2O discrepancies include the AK sample, it appears that AK was also affected by BLF. The similarity between the trends of the AK MIs with the ones expected for HFC could be due to the late entrance of Ti-Mag and apatite to the crystallization path and/or the melt extracted from the boundary layer being less differentiated than in the other volcanic systems.

A BLF model was developed in this study with the aim of illustrating how BLF can produce better fits for minor elements. This model uses rhyolite-MELTS to generate FC models to simulate crystallization in the solidification front, which is extracted and assimilated by the main magma body. More details of this model and results can be found in the Supplementary Material. The model includes the possibility of HFC occurring concurrently to BLF, defined by a factor that indicates the relative amounts of mass fractionated through HFC and BLF. Some crystallization of the main magma body needs to be occurring at the same time of BLF, evidenced by the olivine hosts that trap the evolving melt. The models produced here do not intend to find the best solution for the differentiation process of these MIs but qualitatively illustrate its effect on the liquid lines of decent because there are too many variables to fit, and one BLF model requires many consecutive HFC models to be generated. As rhyolite-MELTS cannot appropriately model hydrous minerals and tends to underestimate apatite crystallization, we only focus on the effect that the BLF models have on TiO_2 and Al_2O_3 (green lines in Figs 9–13). It is seen that the BLF models show a great improvement on the TiO_2 paths while maintaining similar Al_2O_3 paths at higher H_2O for each model.

BLF vs HFC—further distinguishing characteristics supporting solidification fronts

Another important characteristic observed in the HFC models is that the most primitive MIs are in equilibrium with only Ol or close to the Ol-Pl cotectic (most HFC models start by crystallizing only Ol). The

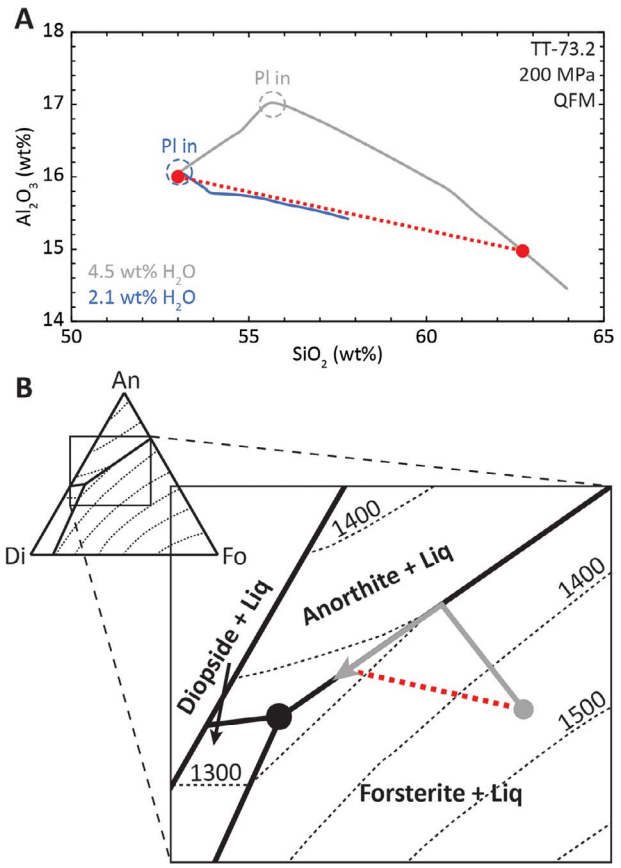

Figure 14 (A) Comparison of HFC trends at low-H_2O, high-H_2O, and mixing trend of primitive and differentiated melts from the high-H_2O model. The HFC models were calculated with rhyolite-MELTS using the composition of TT-73.2. An Al_2O_3 path similar to an HFC path of a low-H_2O melt can be reproduced by BLF or mixing of a high-H_2O melt. (B) Ternary diagram of the Forsterite–Diopside–Anorthite (modified from Morse, 1994) system showing how the BLF produces the melt to evolve towards the eutectic without reaching the Ol-Pl cotectic. Grey line indicates the HFC path and the red dashed line indicates the mixing path for the initial and differentiated melt compositions of the HFC path.

cotectic is not clearly observed by the expected break in the Al_2O_3 trend in the corrected MIs with MIMiC, and it is improbable that for all MI populations found in the tephra samples the most primitive MI reflects the Ol-Pl cotectic. Langmuir (1989) discusses that BLF causes the melt to evolve in the Ol + melt field towards the Ol-Pl-Px cotectic, fractionating all phases in the solidification front but never equilibrating them in the main melt (Fig. 14b). This indicates that there is a higher probability of the primitive MIs actually being in equilibrium with Ol only in addition to having evolved through a BLF path that resembles Pl fractionation. This particular behaviour can have a strong effect on the estimation of primary melt compositions (Kuritani, 1999), which for primitive basalts is usually calculated by addition of equilibrium Ol.

Kuritani (2009) analysed the factors that affect the interplay between HFC and BLF as controls on the fractionation process operating. The preponderance of one process over the other is controlled by the efficiency of transport of the differentiated melt in the solidification front to the main magma body (melt extraction). The efficiency of melt extraction is directly proportional to the density contrast between the main melt and the boundary layer liquid and inversely proportional to the effective viscosity. The effect that water has on melt density and viscosity makes magmatic H_2O content crucially important in controlling the main differentiation process. At pressures above 100 MPa, magmas can contain significant amount of H_2O in undersaturated conditions and water is increasingly concentrated in the boundary layer melt due to high volumes of crystallization. This generates high melt density contrasts and reduces the effective viscosity of the boundary layer melt, promoting melt extraction from the solidification front. When the melt is initially saturated, melt extraction efficiency is reduced because the density contrast decreases as the boundary layer melt does not see a significant increase in H_2O concentrations. Nonetheless, efficiency of melt extraction at saturated conditions may be facilitated by filter-pressing due to bubble formation (Bachmann & Bergantz, 2006).

The increase of water content in the boundary layer melt that is incrementally assimilated by the main melt also hampers crystallization of the main melt by reducing the liquidus temperature as water content increases, further promoting BLF over HFC. In short, the Kuritani (2009) model predicts that BLF is expected to be the main magmatic differentiation process in hydrous basic magmas (>3 wt% H_2O) stored at pressures above 100 MPa, especially at undersaturated conditions. Thus, it can be expected that the pressure-H_2O conditions estimated from the MI data should promote BLF over HFC for all arc melts in northern Japan that we considered in the present study. This is consistent with the behaviour observed for the AK sample. The AK MI trend is closer to a HFC trend than all the other samples and yields the lowest H_2O and pressure estimations of the five samples, which is close to the HFC-BLF transition values modelled by Kuritani (2009).

Another characteristic of volcanic rocks that has been used in support of BLF in solidification fronts is the necessity of fractionation of 'ghost phases' to reproduce the evolution of a magmatic suite (Nielsen & DeLong, 1992). This means that to reproduce the magmatic variation, mineral phases that are not observed in the rocks and that are not predicted to be in equilibrium need to be fractionated. This is due to the high amount of crystallization that occurs in the solidification front, which starts fractionating mineral phases that are never equilibrated with the main magma. Nielsen & DeLong (1992) showed how the late appearance of mineral phases like Ti-Mag and apatite in the crystallization assemblage of the solidification front affect the overall TiO_2 and P_2O_5 trends, respectively, while the main magma body does not equilibrate these phases. As discussed above, the TiO_2 trends indicate fractionation of Fe-Ti oxide minerals even for the samples that do not show any Ti-Mag in the mineral assemblage (AK, HK, and AKN). Further, Na_2O and P_2O_5 sub-horizontal trends in the TT sample indicate fractionation of significant amounts of Na-rich Pl and apatite, which are not observed in the tephra sample and are not expected to be in equilibrium with the TT melt composition.

The presence of compositional signatures of BLF in all the volcanic systems studied here may hint that BLF is the most common differentiation mechanism occurring in the arc front of northern Japan. In volcanic suites where BLF has played a major role during differentiation, the currently common use of simple HFC models has important negative repercussions on volcanic hazards assessments in subduction zone environments. As shown in this study, HFC models typically result in prediction of substantially lower H_2O contents in the melt, which has a substantial effect on predictions of P–T conditions, viscosity estimations and explosivity potential of future eruptions. Estimates of the conditions of magma generation in subduction settings are also strongly affected, as reverse HFC models

are usually applied to backtrack primary magma compositions. More realistic models to estimate primary magma compositions will need to be developed to gain a robust understanding of melt generation in the mantle beneath volcanic arcs.

CONCLUSIONS

In this study, Ol-hosted MI populations of five different volcanic systems along the arc in northern Japan were analysed. The compositional trends of PEC-corrected compositions indicate that most MI populations were completely re-equilibrated to storage conditions prior to eruption.

Estimates of corrected MI compositions indicate that the magmas have H_2O contents ranging from *c*. 3 to *c*. 8 wt%, stored at upper crustal pressures of *c*. 100 to 300 MPa.

An attempt to model the MI differentiation trends by homogeneous fractional crystallization was done using the MushPEC program. Discrepancies of between modelled HFC trends and minor oxide contents in the MIs indicate the involvement of accessory phases (Ti-Mag and apatite) that are not in equilibrium with the melt. The discrepancies between the estimated H_2O contents using Ol-melt hygrometry and MushPEC further corroborates that the observed liquid lines of descent are produced by the interaction of melts of contrasting compositions.

BLF in solidification fronts is proposed as the most probable mechanism of magmatic differentiation, compatible with the observed MI trends. Incremental amounts of differentiated liquid are extracted from the crystalline boundary layer and are assimilated by the main melt. These produce differentiation paths that resemble HFC of low H_2O melts, and with features of fractionation of mineral phases that are never equilibrated by the melts represented in the MIs. These results are also in agreement with model predictions (Kuritani, 2009) that indicate promotion of BLF over HFC in hydrous magmas of >3 wt% H_2O, stored at pressures of >100 MPa.

Given the ubiquity of BLF in solidification fronts at all five arc volcanoes studied, magma differentiation through this process is likely common in the northern Japan arc front. In addition, BLF has previously been invoked to explain the magmatic evolution of other magmatic systems in northern Japan, e.g., in Rishi volcano in the back-arc (Kuritani, 1999) and the Cretaceous Nosappumisaki intrusion (Simura & Ozawa, 2011). The possibility of BLF being the main differentiation mechanism in other subduction zone systems needs to be assessed by the study of arc-related volcanic samples elsewhere. If BLF is common, the application of simple HFC models to understand the magmatic conditions of volcanic systems will yield inaccurate predictions of P–T-H_2O conditions, which would negatively affect the assessment of volcanic hazards, as well as leading to the derivation of inaccurate primary melt compositions.

Funding

This research and the Ph.D. scholarship to R.B. were funded by the Royal Society of New Zealand through the Marsden Fund (MAU1704 to G.F.Z.).

ACKNOWLEDGEMENTS

We want to acknowledge Maxim Gavrilenko and an anonymous reviewer for their helpful comments, and Adam Kent for his comments and editorial duties. Many thanks to Mark Kendrick for providing the used glass standards for volatiles SIMS analysis, to Ian Schipper for the help with the EPMA work at Victoria University, to Paolo Papale for his help answering questions that help for the implementation of his volatile solubility model, to Daniel Rasmussen for his help with the MIMiC script, and to Mattia Pistone for his help with comments and references about mixing dynamics. Special thanks to Hajime Taniuchi for his help with fieldwork in Hokkaido.

REFERENCES

Acocella, V., Yoshida, T., Yamada, R. & Funiciello, F. (2008). Structural control on late Miocene to quaternary volcanism in the NE Honshu arc, Japan. *Tectonics* **27**, 1–24.

Aitchison, J. (1986) *The Statistical Analysis of Compositional Data*. London/New York: Chapman and Hall.

Almeev, R. R., Holtz, F., Koepke, J. & Parat, F. (2012). Experimental calibration of the effect of H_2O on plagioclase crystallization in basaltic melt at 200 MPa. *American Mineralogist* **97**, 1234–1240.

Almeev, R. R., Holtz, F., Koepke, J., Parat, F. & Botcharnikov, R. E. (2007). The effect of H_2O on olivine crystallization in MORB: experimental calibration at 200 MPa. *American Mineralogist* **92**, 670–674.

Ariskin, A. A. & Barmina, G. S. (2004). COMAGMAT: development of a magma crystallization model and its petrological applications. *Geochemistry International* **42**, S1–S157.

Ariskin, A. A., Bychkov, K. A., Nikolaev, G. S. & Barmina, G. S. (2018). The COMAGMAT-5: modeling the effect of Fe–Ni sulfide immiscibility in crystallizing magmas and cumulates. *Journal of Petrology* **59**, 283–298.

Bachmann, O. & Bergantz, G. W. (2004). On the origin of crystal-poor rhyolites: extracted from batholithic crystal mushes. *Journal of Petrology* **45**, 1565–1582.

Bachmann, O. & Bergantz, G. W. (2006). Gas percolation in upper-crustal silicic crystal mushes as a mechanism for upward heat advection and rejuvenation of near-solidus magma bodies. *Journal of Volcanology and Geothermal Research* **149**, 85–102.

Bird, P. (2003). An updated digital model of plate boundaries. *Geochemistry, Geophysics, Geosystems* **4**, 1–52.

Blake, S. (1984). Volatile oversaturation during the evolution of silicic magma chambers as an eruption trigger. *Journal of Geophysical Research: Solid Earth* **89**, 8237–8244.

Blake, S. & Fink, J. H. (1987). The dynamics of magma withdrawal from a density stratified dyke. *Earth and Planetary Science Letters* **85**, 516–524.

Blundy, J., Melekhova, E., Ziberna, L., Humphreys, M. C. S., Cerantola, V., Brooker, R., McCammon, C. A., Pichavant, M. & Ulmer, P. (2020). Effect of redox on Fe-Mg-Mn exchange between olivine and melt and an oxybarometer for basalts. *Contributions to Mineralogy and Petrology* **175**, 103.

Bowen, N. L. (1915). The later stages of the evolution of the igneous rocks. *Geological Magazine* **23**, 1.

Bowen, N. L. (1928). The evolution of the igneous rocks. *Geological Magazine* **66**, 523–525.

Brahm, R., Parada, M. A., Morgado, E., Contreras, C. & McGee, L. E. (2018). Origin of Holocene trachyte lavas of the Quetrupillán volcanic complex, Chile: examples of residual melts in a rejuvenated crystalline mush reservoir. *Journal of Volcanology and Geothermal Research* **357**, 163–176.

Brahm, R., Zellmer, G. F., Kuritani, T., Coulthard, D., Nakagawa, M., Sakamoto, N., Yurimoto, H. & Sato, E. (2021). MushPEC: correcting post-entrapment processes affecting melt inclusions hosted in olivine antecrysts. *Frontiers in Earth Science* **8**, 731.

Browne, B. & Szramek, L. (2015) Rates of Magma Ascent and Storage. In: (Sigurdsson H. (ed)) *The Encyclopedia of Volcanoes*, 2nd edn. Amsterdam: Academic Press, pp.203–214.

Danyushevsky, L. V. (2001). The effect of small amounts of H_2O on crystallisation of mid-ocean ridge and backarc basin magmas. *Journal of Volcanology and Geothermal Research* **110**, 265–280.

Danyushevsky, L. V., Della-Pasqua, F. N. & Sokolov, S. (2000). Re-equilibration of melt inclusions trapped by magnesian olivine phenocrysts from subduction-related magmas: petrological implications. *Contributions to Mineralogy and Petrology* **138**, 68–83.

Danyushevsky, L. V., Leslie, R. A. J., Crawford, A. J. & Durance, P. (2004). Melt inclusions in primitive olivine phenocrysts: the role of localized reaction processes in the origin of anomalous compositions. *Journal of Petrology* **45**, 2531–2553.

Danyushevsky, L. V., McNeill, A. W. & Sobolev, A. V. (2002). Experimental and petrological studies of melt inclusions in phenocrysts from mantle-derived magmas: an overview of techniques, advantages and complications. *Chemical Geology* **183**, 5–24.

Danyushevsky, L. V. & Plechov, P. (2011). Petrolog3: integrated software for modeling crystallization processes. *Geochemistry, Geophysics, Geosystems* **12**, 1–32.

Dufek, J. & Bachmann, O. (2010). Quantum magmatism: magmatic compositional gaps generated by melt-crystal dynamics. *Geology* **38**, 687–690.

Forni, F., Bachmann, O., Mollo, S., De Astis, G., Gelman, S. E. & Ellis, B. S. (2016). The origin of a zoned ignimbrite: insights into the Campanian ignimbrite magma chamber (Campi Flegrei, Italy). *Earth and Planetary Science Letters* **449**, 259–271.

Frost, T. P. & Mahood, G. A. (1987). Field, chemical, and physical constraints on mafic-felsic magma interaction in the Lamarck granodiorite, Sierra Nevada, California. *GSA Bulletin* **99**, 272–291.

Fujinawa, A., Iwasaki, M., Honda, K., Nagao, A. & Wachi, T. (2004). Eruption history in the post-caldera stage of Akita-Komagatake volcano, northeastern Japan arc: correlation between eruptives constituting volcanic edifices and air-fall tephra layers. *Kazan* **49**, 333–354.

Gavrilenko, M., Herzberg, C., Vidito, C., Carr, M. J., Tenner, T. & Ozerov, A. (2016a). A calcium-in-olivine Geohygrometer and its application to subduction zone magmatism. *Journal of Petrology* **57**, 1811–1832.

Gavrilenko, M., Ozerov, A., Kyle, P. R., Carr, M. J., Nikulin, A., Vidito, C. & Danyushevsky, L. (2016b). Abrupt transition from fractional crystallization to magma mixing at Gorely volcano (Kamchatka) after caldera collapse. *Bulletin of Volcanology* **78**, 1–28.

Gelman, S. E., Deering, C. D., Gutierrez, F. J. & Bachmann, O. (2013). Evolution of the Taupo volcanic center, New Zealand: petrological and thermal constraints from the omega dacite. *Contributions to Mineralogy and Petrology* **166**, 1355–1374.

Ghiorso, M. S., Hirschmann, M. M., Reiners, P. W. & Kress, V. C. (2002). The pMELTS: a revision of MELTS for improved calculation of phase relations and major element partitioning related to partial melting of the mantle to 3 GPa. *Geochemistry, Geophysics, Geosystems* **3**, 1030.

Ghiorso, M. S. & Sack, R. O. (1995). Chemical mass transfer in magmatic processes IV. A revised and internally consistent thermodynamic model for the interpolation and extrapolation of liquid-solid equilibria in magmatic systems at elevated temperatures and pressures. *Contributions to Mineralogy and Petrology* **119**, 197–212.

Gonnermann, H. M. (2015). Magma fragmentation. *Annual Review of Earth and Planetary Sciences* **43**, 431–458.

Grove, T. L. & Kinzler, R. J. (1986). Petrogenesis of andesites. *Annual Review of Earth & Planetary Sciences* **14**, 417–454.

Gualda, G. A. R., Ghiorso, M. S., Lemons, R. V. & Carley, T. L. (2012). Rhyolite-MELTS: a modified calibration of MELTS optimized for silica-rich, fluid-bearing magmatic systems. *Journal of Petrology* **53**, 875–890.

Harker, A. (1909) *The Natural History of Igneous Rocks*. Cambridge: Cambridge University Press.

Hartley, M. E., Neave, D. A., Maclennan, J., Edmonds, M. & Thordarson, T. (2015). Diffusive over-hydration of olivine-hosted melt inclusions. *Earth and Planetary Science Letters* **425**, 168–178.

Hughes, E. C., Buse, B., Kearns, S. L., Blundy, J. D., Kilgour, G. & Mader, H. M. (2019). Low analytical totals in EPMA of hydrous silicate glass due to sub-surface charging: obtaining accurate volatiles by difference. *Chemical Geology* **505**, 48–56.

Ishizuka, Y., Nakagawa, M. & Fujiwara, S. y. (2010) *Geological Map of Tokachidake Volcano. Geological Map of Volcanoes*. Geological Survey of Japan, AIST, Tsukuba, Japan.

Itaya, T., Nagao, K., Nishido, H. & Ogata, K. (1984). K-Ar age determination of late pleistocene volcanic rocks. *The Journal of the Geological Society of Japan* **90**, 899–909.

Jerram, D. A. & Martin, V. M. (2008). Understanding crystal populations and their significance through the magma plumbing system. *Geological Society, London, Special Publications* **304**, 133.

Kelley, K. A., Plank, T., Grove, T. L., Stolper, E. M., Newman, S. & Hauri, E. (2006). Mantle melting as a function of water content beneath back-arc basins. *Journal of Geophysical Research: Solid Earth* **111**, 1–27.

Kendrick, M. A., Hémond, C., Kamenetsky, V. S., Danyushevsky, L., Devey, C. W., Rodemann, T., Jackson, M. G. & Perfit, M. R. (2017). Seawater cycled throughout Earth's mantle in partially serpentinized lithosphere. *Nature Geoscience* **10**, 222–228.

Kimura, G. (1996). Collision orogeny at arc-arc junctions in the Japanese Islands. *Island Arc* **5**, 262–275.

Kimura, J. I. & Ariskin, A. A. (2014). Calculation of water-bearing primary basalt and estimation of source mantle conditions beneath arcs: PRIMACALC2 model for WINDOWS. *Geochemistry, Geophysics, Geosystems* **15**, 1494–1514.

Kita, S., Hasegawa, A., Nakajima, J., Okada, T., Matsuzawa, T. & Katsumata, K. (2012). High-resolution seismic velocity structure beneath the Hokkaido corner, northern Japan: arc-arc collision and origins of the 1970 M 6.7 Hidaka and 1982 M 7.1 Urakawa-oki earthquakes. *Journal of Geophysical Research B: Solid Earth* **117**, 1–23.

Kita, S., Nakajima, J., Hasegawa, A., Okada, T., Katsumata, K., Asano, Y. & Kimura, T. (2014). Detailed seismic attenuation structure beneath Hokkaido, northeastern Japan: arc-arc collision process, arc magmatism, and seismotectonics. *Journal of Geophysical Research: Solid Earth* **119**, 6486–6511.

Kudo, T. & Hoshizumi, H. (2006) *Catalog of Eruptive Events within the Last 10,000 Years in Japan, Database of Japanese Active Volcanoes*. Geological Survey of Japan, AIST, Tsukuba, Japan.

Kudo, T., Okuno, M. & Nakamura, T. (2003). Eruptive history of Kita-Hakkoda volcanic group during the last 6000 years, Northeast Japan. *Chishitsugaku Zasshi =Journal of the Geological Society of Japan* **109**, 151–165.

Kudo, T., Okuno, M., Ohba, T., Kitade, Y. & Nakamura, T. (2000). The eruptive products from Jigoku-numa hot pool in Kita-Hakkoda volcano group, Northeast Japan: eruption style, magnitude and age. *Kazan* **45**, 315–322.

Kudo, T., Takarada, S. & Sasaki, M. (2004). Geology and volcanic history of Kita-Hakkoda volcanic group, Northeast Japan. *Journal of the Geological Society of Japan* **110**, 271–289.

Kuritani, T. (1999). Thermal and compositional evolution of a cooling magma chamber by boundary layer fractionation: model and its application for primary magma estimation. *Geophysical Research Letters* **26**, 2029–2032.

Kuritani, T. (2009). The relative roles of boundary layer fractionation and homogeneous fractionation in cooling basaltic magma chambers. *Lithos* **110**, 247–261.

Kuritani, T., Kanai, C., Yamashita, S. & Nakagawa, M. (2019). Magma generation conditions at the Akita-Komagatake volcano, Northeast Japan arc: implications of across-arc variations in mantle melting parameters. *Lithos* **348–349**, 105197.

Kuritani, T., Tanaka, M., Yokoyama, T., Nakagawa, M. & Matsumoto, A. (2016). Intensive hydration of the wedge mantle at the Kuril arc-NE Japan arc junction: implications from mafic lavas from Usu volcano, northern Japan. *Journal of Petrology* **57**, 1223–1240.

Kuritani, T., Yokoyama, T. & Nakamura, E. (2008). Generation of rear-arc magmas induced by influx of slab-derived supercritical liquids: implications from alkali basalt lavas from Rishiri volcano, Kurile arc. *Journal of Petrology* **49**, 1319–1342.

Langmuir, C. H. (1989). Geochemical consequences of *in situ* crystallization. *Nature* **340**, 199–205.

Liao, Y., Wei, C. & Rehman, H. U. (2021). Titanium in calcium amphibole: behavior and thermometry. *American Mineralogist* **106**, 180–191.

Maclennan, J. (2017). Bubble formation and decrepitation control the CO_2 content of olivine-hosted melt inclusions. *Geochemistry, Geophysics, Geosystems* **18**, 597–616.

Markhinin, E. K., Anikiev, Y. A. & Grannik, V. M. (1974). The eruption of Tyatya volcano on the Kuril Islands in July 1973. *Geologiya I Geofizika* **10S**, 20–31.

Marsh, B. D. (1996). Solidification fronts and magmatic evolution. *Mineralogical Magazine* **60**, 5–40.

Marsh, B. D. (2007) Magmatism, magma, and magma chambers. In: (Schubert G. (ed)) *Treatise on Geophysics*. Amsterdam: Elsevier, pp.275–333.

Martin, A. K. (2011). Double saloon door tectonics in the Japan Sea, fossa magna, and the Japanese Island arc. *Tectonophysics* **498**, 45–65.

Médard, E. & Grove, T. L. (2008). The effect of H_2O on the olivine liquidus of basaltic melts: experiments and thermodynamic models. *Contributions to Mineralogy and Petrology* **155**, 417–432.

Molina, J. F., Scarrow, J. H., Montero, P. G. & Bea, F. (2009). High-Ti amphibole as a petrogenetic indicator of magma chemistry: evidence for mildly alkalic-hybrid melts during evolution of Variscan basic–ultrabasic magmatism of Central Iberia. *Contributions to Mineralogy and Petrology* **158**, 69–98.

Mollo, S., Giacomoni, P. P., Coltorti, M., Ferlito, C., Iezzi, G. & Scarlato, P. (2015). Reconstruction of magmatic variables governing recent Etnean eruptions: constraints from mineral chemistry and P–T–fO_2–H_2O modeling. *Lithos* **212–215**, 311–320.

Morse, S. A. (1994) *Basalts and Phase Diagrams: An Introduction to the Quantitative use of Phase Diagrams in Igneous Petrology*. Melbourne (Florida, USA): Krieger.

Nakagawa, M. (1985). Geochemical study of lavas from Akita-Komagatake volcano, Northeast Japan-chemical compositional variation of island-arc tholeiitic series. *Res. Rep. Lab. Nuc. Sci. Tohoku Univ.* **18**, 351–365.

Nakagawa, M., Ishizuka, Y., Kudo, T., Yoshimoto, M., Hirose, W., Ishizaki, Y., Gouchi, N., Katsui, Y., Solovyow, A. W., Steinberg, G. S. & Abdurakhmanov, A. I. (2002). Tyatya volcano, southwestern Kuril arc: recent eruptive activity inferred from widespread tephra. *Island Arc* **11**, 236–254.

Nakagawa, M., Matsumoto, A., Kobayashi, K. & Wada, K. (2019). Comparative petrological studies of 1962 and 1988–1989 eruptions of Tokachidake volcano, Japan: a case study for understanding the relationship between eruption style and magma processes. *Journal of Disaster Research* **14**, 766–779.

Newcombe, M. E., Fabbrizio, A., Zhang, Y., Ma, C., Le Voyer, M., Guan, Y., Eiler, J. M., Saal, A. E. & Stolper, E. M. (2014). Chemical zonation in olivine-hosted melt inclusions. *Contributions to Mineralogy and Petrology* **168**, 1030.

Newman, S. & Lowenstern, J. B. (2002). VOLATILECALC: a silicate melt-H_2O-CO_2 solution model written in visual basic for excel. *Computers and Geosciences* **28**, 597–604.

Nielsen, R. L. (1990) Modern methods of igneous petrology. In: (James N. & Kelly R. (eds)) *Simulation of Igneous Differentiation Processes*. Berlin, Boston: De Gruyter, pp.65–106.

Nielsen, R. L. & DeLong, S. E. (1992). A numerical approach to boundary layer fractionation: application to differentiation in natural magma systems. *Contributions to Mineralogy and Petrology* **110**, 355–369.

Northrup, C. J., Royden, L. H. & Burchfie, B. C. (1995). Motion of the Pacific plate relative to Eurasia and its potential relation to Cenozoic extension along the eastern margin of Eurasia. *Geology* **23**, 719–722.

O'Hara, M. J. & Fry, N. (1996). Geochemical effects of small packet crystallization in large magma chambers—further resolution of the highly compatible element paradox. *Journal of Petrology* **37**, 891–925.

Papale, P., Moretti, R. & Barbato, D. (2006). The compositional dependence of the saturation surface of $H_2O + CO_2$ fluids in silicate melts. *Chemical Geology* **229**, 78–95.

Parman, S. W., Grove, T. L., Kelley, K. A. & Plank, T. (2011). Along-arc variations in the pre-eruptive H2O contents of mariana arc magmas inferred from fractionation paths. *Journal of Petrology* **52**, 257–278.

Petrelli, M., El Omari, K., Spina, L., Le Guer, Y., La Spina, G. & Perugini, D. (2018). Timescales of water accumulation in magmas and implications for short warning times of explosive eruptions. *Nature Communications* **9**, 770.

Pistone, M., Blundy, J. & Brooker, R. A. (2017). Water transfer during magma mixing events: insights into crystal mush rejuvenation and melt extraction processes. *American Mineralogist* **102**, 766–776.

Portnyagin, M., Duggen, S., Hauff, F., Mironov, N., Bindeman, I., Thirlwall, M. & Hoernle, K. (2015). Geochemistry of the late Holocene rocks from the Tolbachik volcanic field, Kamchatka: quantitative modelling of subduction-related open magmatic systems. *Journal of Volcanology and Geothermal Research* **307**, 133–155.

Portnyagin, M., Mironov, N., Botcharnikov, R., Gurenko, A., Almeev, R. R., Luft, C. & Holtz, F. (2019). Dehydration of melt inclusions in olivine and implications for the origin of silica-undersaturated island-arc melts. *Earth and Planetary Science Letters* **517**, 95–105.

Putirka, K. D. & Tepley III, F. J. (2008) Thermometers and barometers for volcanic systems. *Reviews in Mineralogy and Geochemistry* **69**, 61–120.

Putirka, K. D., Perfit, M., Ryerson, F. J. & Jackson, M. G. (2007). Ambient and excess mantle temperatures, olivine thermometry, and active vs. passive upwelling. *Chemical Geology* **241**, 177–206.

Rasmussen, D. J., Plank, T. A., Wallace, P. J., Newcombe, M. E. & Lowenstern, J. B. (2020). Vapor-bubble growth in olivine-hosted melt inclusions. *American Mineralogist* **105**, 1898–1919.

Roedder, E. (1979). Origin and significance of magmatic inclusions. *Bulletin de Mineralogie* **102**, 487–510.

Rowe, M. C., Peate, D. W. & Newbrough, A. (2011). Compositional and thermal evolution of olivine-hosted melt inclusions in small-volume basaltic eruptions: a "simple" example from Dotsero volcano, NW Colorado. *Contributions to Mineralogy and Petrology* **161**, 197–211.

Sasaki, Y. (1986). Geochemical study of the eruptive rocks of stage 1 and stage 2 in Hakkoda volcanic group. *Research Report of the Laboratory of Nuclear Science of Tohoku University* **19**, 288–299.

Sasaki, Y. (1987). Geochemical study of the tholeiitic magma of stage 1 in Hakkoda volcanic group. *Research Report of the Laboratory of Nuclear Science of Tohoku University* **20**, 363–374.

Sasaki, Y., Yoshida, T. & Aoki, K. (1985). Geochemistry of Kita-Hakkoda volcanic group, northeastern Japan. *Research Report of the Laboratory of Nuclear Science, Tohoku University* **18**, 175–188.

Sato, E. & Sato, H. (2009). Study of effect of magma pocket on mixing of two magmas with different viscosities and densities by analogue experiments. *Journal of Volcanology and Geothermal Research* **181**, 115–123.

Simura, R. & Ozawa, K. (2011). Magmatic fractionation by compositional convection in a sheet-like magma body: constraints from the Nosappumisaki intrusion, northern Japan. *Journal of Petrology* **52**, 1887–1925.

Sisson, T. W. & Grove, T. L. (1993). Experimental investigations of the role of H_2O in calc-alkaline differentiation and subduction zone magmatism. *Contributions to Mineralogy and Petrology* **113**, 143–166.

Sparks, R. S. J. & Marshall, L. A. (1986). Thermal and mechanical constraints on mixing between mafic and silicic magmas. *Journal of Volcanology and Geothermal Research* **29**, 99–124.

Sutō, S. & Ishii, T. (1987). Geology of the Shizukuishi district. Geological Survey of Japan, AIST, Tsukuba, Japan

Takarada, S. & Muraoka, H. (2004). Geology of the Hakkoda San District. *Quadrangle Series* **1**, 1–86.

Toplis, M. J. (2005). The thermodynamics of iron and magnesium partitioning between olivine and liquid: criteria for assessing and predicting equilibrium in natural and experimental systems. *Contributions to Mineralogy and Petrology* **149**, 22–39.

Turner, M., Turner, S., Blatter, D., Maury, R., Perfit, M. & Yogodzinski, G. (2017a). Water contents of clinopyroxenes from sub-arc mantle peridotites. *Island Arc* **26**, 1–10.

Turner, M., Turner, S., Mironov, N., Portnyagin, M. & Hoernle, K. (2017b). Can magmatic water contents be estimated from clinopyroxene phenocrysts in some lavas? A case study with implications for the origin of the Azores Islands. *Chemical Geology* **466**, 436–445.

Ueki, K. & Iwamori, H. (2017). Geochemical differentiation processes for arc magma of the Sengan volcanic cluster, northeastern Japan, constrained from principal component analysis. *Lithos* **290–291**, 60–75.

Wachi, T. & Koshiya, S. (1997). Tephra stratigraphy and eruptive activities of the Akita-Komagatake volcano. *Kazan* **42**, 17–34.

Wada, K. (1997). Eruption history of me-akan volcano, eastern Hokkaido, during the last 12000 years. The Volcanological Society of Japan 1997 Fall Meeting. https://doi.org/10.18940/vsj.1997.2.0_100.

Wada, K., Ikegami, H. & Inaba, T. (1998). Chemical compositions of the rocks from me-akan volcano eastern Hokkaido Japan: compositional variety of eruptive magmas. *Rep. Taisetsuzan Inst. Sci.* **32**, 43–59.

Wallace, P. J., Kamenetsky, V. S. & Cervantes, P. (2015). Melt inclusion CO_2 contents, pressures of olivine crystallization, and the problem of shrinkage bubbles. *American Mineralogist* **100**, 787–794.

Watanabe, S., Widom, E., Ui, T., Miyaji, N. & Roberts, A. M. (2006). The evolution of a chemically zoned magma chamber: the 1707 eruption of Fuji volcano, Japan. *Journal of Volcanology and Geothermal Research* **152**, 1–19.

Waters, L. E. & Lange, R. A. (2015). An updated calibration of the plagioclase-liquid hygrometer-thermometer applicable to basalts through rhyolites. *American Mineralogist* **100**, 2172–2184.

Wilson, M. (1995). Magmatic differentiation. *Geological Society, London, Memoirs* **16**, 205–218.

Wotzlaw, J.-F., Bindeman, I. N., Watts, K. E., Schmitt, A. K., Caricchi, L. & Schaltegger, U. (2014). Linking rapid magma reservoir assembly and eruption trigger mechanisms at evolved Yellowstone-type supervolcanoes. *Geology* **42**, 807–810.

Yokoyama, I., Katsui, Y., Ehara, S. & Koide, K. (1976) *Meakandake. Volcano Geology, Eruption History, Current Activities and Disaster Prevention Measures (in Japanese)*. Sapporo: Hokkaido Disaster Management Council.

Yoshida, T. & Aoki, K. I. (1984). Geochemistry of major and trace elements in the quaternary volcanic rocks from Northeast Honshu, Japan. *Science Reports of the Tohoku Imperial University, 3rd Series* **16**, 1–34.

Yoshida, T., Kimura, J. I., Yamada, R., Acocella, V., Sato, H., Zhao, D., Nakajima, J., Hasegawa, A., Okada, T., Honda, S., Ishikawa, M., Ardiansyah Prima, O. D., Kudo, T., Shibazaki, B., Tanaka, A. & Imaizumi, T. (2014). Evolution of late cenozoic magmatism and the crust-mantle structure in the NE japan arc. *Geological Society Special Publication* **385**, 335–387.

Zellmer, G. F., Pistone, M., Iizuka, Y., Andrews, B. J., Gomez-Tuena, A., Straub, S. M. & Cottrell, E. (2016). Petrogenesis of antecryst-bearing arc basalts from the trans-Mexican Volcanic Belt: insights into along-arc variations in magma-mush ponding depths, H2O contents, and surface heat flux. *American Mineralogist* **101**, 2405–2422.

Zellmer, G. F., Sakamoto, N., Iizuka, Y., Miyoshi, M., Tamura, Y., Hsieh, H. H. & Yurimoto, H. (2014). Crystal uptake into aphyric arc melts: insights from two-pyroxene pseudo-decompression paths, plagioclase hygrometry, and measurement of hydrogen in olivines from mafic volcanics of SW Japan. *Geological Society Special Publication* **385**, 161–184.

Zen, E.-A. (1986). Aluminum enrichment in silicate melts by fractional crystallization: some mineralogic and petrographic constraints. *Journal of Petrology* **27**, 1095–1117.